Automated neuronal reconstruction with super-multicolour fluorescence imaging

Marcus N. Leiwe[1,2], Satoshi Fujimoto[1,2], Toshikazu Baba[1,2], Daichi Moriyasu[1], Biswanath Saha[1], Richi Sakaguchi[1], Shigenori Inagaki[1], & Takeshi Imai[1,2]*

Affiliations:
[1] Graduate School of Medical Sciences, Kyushu University, Fukuoka 812-8582, Japan.
[2] These authors contributed equally.
*e-mail: imai.takeshi.457@m.kyushu-u.ac.jp

ABSTRACT

Fluorescence imaging is widely used for the mesoscopic mapping of neuronal connectivity. However, neurite reconstruction is challenging, especially when neurons are densely labelled. Here we report a strategy for the fully automated reconstruction of densely labelled neuronal circuits. Firstly, we established stochastic "super-multicolour" labelling with up to seven different fluorescent proteins using the Tetbow method. With this method, each neuron was labelled with a unique combination of fluorescent proteins, which were then imaged and separated by linear unmixing. We also established an automated neurite reconstruction pipeline based on the quantitative analysis of multiple dyes (QDyeFinder). To classify colour combinations, we used a newly developed unsupervised clustering algorithm, dCrawler, in which data points in multi-dimensional space were clustered based on a given threshold distance. Our new strategy allows for the reconstruction of neurites for up to hundreds of neurons at a millimetre scale without manual tracing.

MAIN

The brain is made up of dense networks of interconnected neurons. Mapping the anatomy of these dense networks is one of the biggest challenges in neuroscience. Electron microscopy (EM) provides the synaptic resolution and is used as a gold standard in connectomics [1, 2]. It is now possible to obtain EM images for 1 mm^3 volumes (~petabyte scale) [3, 4]; however, due to its extremely large data size, the reconstruction process is the bottle neck. Light microscopy (LM) is useful for the mesoscopic circuit mapping at a whole-brain level [5-9]. However, the reconstruction of densely labelled circuits is challenging as its limited resolution hinders the discrimination of thin axonal fibres (down to ~100 nm) originating from different neurons. It is, therefore, essential to limit the number of labelled neurons in single-cell reconstruction in LM. Moreover, manual circuit tracing is a highly laborious and rate limiting step in large-scale circuit reconstruction with LM. For both EM and LM connectomics, current reconstruction strategies are all based on the continuity of the target structure; we, therefore, cannot reconstruct the neurites correctly once we lose just a few sections of the images. In theory, error rates in reconstruction exponentially increase as the length of the neurites increases. Thus, connectomics beyond a millimetre scale remains a big challenge.

To improve the discriminability of neurites in a densely labelled circuits, it is effective to utilize the colour information in LM. For example, if we utilize the combination of three

colours (red, green, and blue), ~20 different lines can be easily dissociable in a Tokyo railway map (Fig. 1a). Similarly, multicolour labelling is useful for LM-based circuit reconstruction in the brain. Stochastic multicolour labelling strategies, such as Brainbow, utilize a combination of 3 fluorescent proteins (XFPs) to create different colour hues [10, 11]. A brighter version of this method, Tetbow [12], allows for multicolour fluorescence imaging in 3D in combination with tissue clearing with SeeDB2 [13]. However, the combination of three colours only produces ~20 discernible colour hues [12], which falls well short of the variations necessary to reconstruct densely labelled neuronal circuits.

In this study, we performed "super-multicolour" labelling of neuronal circuits, in which >3 XFPs were utilized to expand colour combinations. However, we cannot recognize the combination of >3 colours visually, as most humans only have trichromatic colour vision. We, therefore, developed a fully automated neurite reconstruction pipeline based on quantitative analysis of multiple dyes (QDyeFinder). In this pipeline, we identified neurites for different neurons based on colour information only. The combination of super-multicolour labelling and the QDyeFinder pipeline facilitates automated circuit reconstruction beyond a millimetre scale without tedious manual tracing.

RESULTS

Super-multicolour imaging with 7 XFPs and linear unmixing

Stochastic multicolour labelling of neurons (e.g., Brainbow) typically utilizes only 3 XFPs [11]. This is simply because it is difficult to identify >3 colours in the merged images visually. However, the possible combinations or "colour hues" will increase by utilizing more colours [14, 15]. We, therefore, aimed for "super-multicolour" fluorescence labelling utilizing >3 types of XFPs.

Firstly, we screened for XFPs which are bright, monomeric, evenly distributed in mammalian neurons, excitable with conventional laser lines, and are spectrally dissimilar to each other. We identified a combination of 7 XFPs that met all the above criteria: mTagBFP2, mTurquoise2, and mAmetrine1.1 were excitable with 405 nm laser; mNeonGreen and YPet were excitable with 488 nm laser; mRuby3 and tdKatushka2 were excitable with 552 nm laser (Fig. 1b). We excluded XFPs that were prone to aggregation, photobleaching, and/or distributing unevenly in neurites. Emission signals for different XFPs were separated by diffraction gratings during confocal imaging.

When multiple types of XFPs are excited with a single laser, the emission spectra partially overlap with each other. To extract the fluorescence signals derived from a single type of XFP, we used linear unmixing [16, 17]. For successful linear unmixing, the linearity of the fluorescence signal is critical. When detectors of the confocal microscope are not sufficiently linear (e.g., Leica HyD detectors [18, 19]), we have to correct the linearity to improve the performance of linear unmixing (Extended Data Fig. 1). Then, using HEK293T cells expressing a single type of XFPs, we determined how much signals leaks into different channels. Based on this reference data, we calculated how much signals are derived from each of the XFPs (Extended Data Fig. 2). In this way, 2 or 3 XFPs excited with the same laser line were fully separated after linear unmixing (Fig. 1c). Thus, we can obtain fluorescence signals for up to 7 XFPs separately with conventional laser lines in confocal microscopy.

We previously reported the bright and stochastic multicolour labelling method, Tetbow [12]. With Tetbow, tTA and TRE-XFP vectors are stochastically introduced into neurons. As each of the XFP genes are encoded in different plasmids or adeno-associated virus (AAVs), it is easy to increase the number of XFPs. Following the same condition as in the original study, we established 7-colour Tetbow in the mouse brain. Using *in utero* electroporation at E15, L2/3 neurons in the primary somatosensory cortex (S1) was labelled with 7-colour Tetbow (Fig. 1d). After 7-colour imaging and linear unmixing, we observed the combinatorial expression of 7 different XFPs. Both axons and dendrites were brightly labelled with these XFPs.

7-colour Tetbow provides superior discriminability of neurons based on colour hues

Our trichromatic colour vision can only recognize the combination of 3 channels, namely red, green, and blue. To quantitatively evaluate colour hues produced by ≥3 channels of the fluorescence signals, we need to introduce a numerical description of the colour hues that can also be extended to N channel images. Fluorescence intensities in the N channel images can be plotted in the N-dimensional space. After normalizing values across N channels (normalized to the maximum ROI value), we obtained vector-normalized intensity values (designated "colour vector", hereafter). The colour vector data will be plotted on the surface of the hyperplane in the N-dimensional space (Extended Data Fig. 3a). One easy way to assess the colour hue similarity is to calculate the Euclidean distance (*d*) between the colour vectors. The more similar the colour hues are, the shorter the *d* value will be. We can also evaluate colour hue discriminability in this scheme. We can judge discriminable when distance between the two colour vectors is above a defined threshold value, *Th(d)* (Fig. 2a).

Firstly, we examined whether neurons labelled with 7-colour Tetbow are more discriminable than the conventional 3-colour Tetbow. To compare the discrimination performance in the same condition, we utilized synthetic datasets. As the copy number of introduced XFP expression vectors follows a Poisson's distribution in Tetbow, we can simulate the expression patterns of XFPs [12] (Extended Data Fig. 3b). We simulated the expression profiles under the condition of an average of 0.1-6 gene copies / cell / colour. We compared synthetic data for 3- vs. 7-colour Tetbow. When an average of 2 copies / cell / colour was introduced, for example, only 93% of neuronal pairs were discriminable at *Th(d)* = 0.2 with 3-colour Tetbow; however, >99.9% of neuronal pairs were discriminable with 7-colour Tetbow at the same threshold (Fig. 2b and Extended Data Fig. 3c).

This does not mean that all of the 1000 neurons are fully separated because of the "birthday problem" [20]. We estimated the fraction of "uniquely-labelled neurons", which are separated by >*Th(d)* from any other neurons (Fig. 2c). Using Monte-Carlo simulations with various numbers of cells, we calculated what percentage of cells would be uniquely labelled at different *Th(d)* values. We found that 93.3% of neurons are uniquely labelled when 100 neurons are labelled (and 86.3% for 200 cells) with 7-colour Tetbow and *Th(d)* = 0.2 (Fig. 2d and Extended Data Fig. 3d).

Next, we evaluated colour discriminability with 7-colour Tetbow using the real samples. Layer 2/3 neurons in S1 were labelled with the 7-colour Tetbow using *in utero* electroporation. Four-week-old brain samples were cleared with SeeDB2G [13], and 7-channel images were obtained with confocal microscopy followed by linear unmixing. Fluorescence signals isolated from 2031 somata were analysed for colour vector similarity (Fig. 2e). We found that 99.7% of neuronal pairs were discriminable at *Th(d)* = 0.2 (Fig. 2f), which is much

better than the 3-colour Tetbow (64.5%) [12]. In this condition, 79% out of 100 neurons can be uniquely labelled (Fig. 2g).

Strategy for automated neurite reconstructions based on colour hue similarity

As many of neurons are uniquely labelled by the combinatorial expression of 7 XFPs, we considered that we should be able to identify neurites for different neurons solely based on the colour hue information. This will be conceptually different from existing neurite reconstruction strategy which is based on the physical continuity of the neurites (neurite "tracing") [21-25]. Thus, our new strategy could overcome the limitation of the existing reconstruction methods.

Colour hue similarity can be evaluated based on the Euclidean distance between colour vectors in the 7-dimensional space as described in Fig. 2a. We initially tried to evaluate colour vector for each pixel. However, it was difficult for two reasons. Firstly, the colour vector was not stable enough at the single pixel level. Shot noise contributed to significant fluctuations. Furthermore, the distribution of XFPs were not completely uniform at a local level (< several microns) especially in thin axons. Secondly, pixel-based analysis required a massive amount of machine power for pairwise distance calculations, hampering analysis of gigabyte-scale images. We, therefore, decided to extract colour vector data for regions of interest (ROIs) consisting of multiple pixels.

We thus needed to set ROIs for neurites. There are many open source and commercialized software to automatically detect fibrous structures such as neurites. They cannot trace neurites entirely but are good enough to detect many of the bright neurite fragments. We used one of them, Neurolucida 360 [22], to automatically detect neurite fragments.

Briefly, we obtained fluorescence intensity values from each of the neurite fragments as ROIs and obtained colour vector data. We then performed unsupervised clustering of the colour vector data for all of the ROIs. If neurites from the same neuron have very similar colour hues, each cluster should represent neurites from the same neuron. In this way, we established an automated neurite reconstruction pipeline based on quantitative analysis of multiple dyes (QDyeFinder) (Fig. 3).

QDyeFinder pipeline and quality control

Here we describe the more details of the QDyeFinder pipeline, including pre-processing, parameter setting, and quality control (QC) procedures.

Firstly, after obtaining N-channel fluorescence images, we performed linear unmixing as described in Fig. 1. To obtain N-channel signals accurately from thin neurites, it is important to minimize chromatic aberrations. When necessary, we performed *post-hoc* correction of chromatic aberrations as described previously [26] (Fig. 3a).

Next, we generated channel-stacked images and automatically detected neurite fragments using Neurolucida 360. This software can detect bright neurite fragments with sufficient signal-to-noise ratios but cannot fully trace neurites with dim compartments. Existing neurite detection software including Neurolucida 360 often make mistakes when neurites are making branches and/or multiple neurites are crossing over along *z*. We,

therefore, broke the detected fragments down to smaller fragments at branch and crossing-over points (Fig. 3b). These fragments were used as ROIs in subsequent analyses.

We obtained mean intensity values for N channels in each of the ROIs. As a part of QC, we examined whether all the N channels have sufficient signal-to-noise (S/N) ratios. We determined cumulative plots for signal intensities in the ROIs and background (non-ROI areas). We checked if all of the channels have sufficient S/N at the 80-100 percentile range of the intensities. We need to discard the channel when S/N in this range was <2.5, as we cannot expect reliable signals for that channel (Extended Data Fig.4a). There may be no or little label for that channel, in that case.

We also needed to discard very short neurite fragments, as the colour vector data becomes less stable as the length decreases. We used neurite fragment data from 7-colour Tetbow samples (L2/3 neurons in S1, imaged with a 63x lens) to evaluate this issue. Neurite fragments were artificially broken down to smaller sub-fragments of varying lengths. To examine the relationship between length and colour vector stability we measured the Euclidean distance (*d*) between the sub-fragments the parental (whole) fragment. We found that $d > 0.1$ when the lengths of sub-fragments become <5 μm (Supplementary Fig. 4b). We, thus, decided to consider ROIs at a length of >5 μm for this image.

We also discarded ROIs with insufficient brightness. There is a trade-off between the brightness and reliability of the colour vectors, where neurites that are dim produce unreliable colour vectors. We split each neurite fragment into sub-fragments of the minimum length and calculated the Euclidean distance (*d*) of the colour vector to that of the parental fragment. If $d > 0.2$, we defined it as an inaccurate sub-fragment. To determine a magnitude threshold, we found the smallest magnitude cut-off where less than 5% of the sub-fragments were inaccurate. We then excluded ROIs whose channel-stacked signals are below the defined threshold brightness, 0.1 (Extended Data Fig. 4c).

While we broke fragments at the branch and crossing-over points, the Neurolucida 360 software can still make mistakes for neurite identification. If the colour hue abruptly changes in the middle of the fragment, then detected fragment is most likely a “wrong” hybrid of different neurites that intersect. We, therefore, broke down the fragments further when the colour vectors in adjacent sub-fragments (segmenting by the minimum fragment length described above) of the fragment are separated by $d > 0.3$ (Extended Data Fig. 4d).

With all the ROIs with reliable signals, the mean intensity values were extracted and then vector normalized to obtain the final colour vectors. We next performed unsupervised clustering of colour vectors. Ideally, each of the cluster should represent neurite fragments from a single neuron (Fig. 3d). Clustering algorithm and its parameter setting are critical for accurate classification.

dCrawler: A threshold distance-based unsupervised clustering

Various types of algorithms are known for unsupervised clustering (Extended Data Table 1). For example, k-means clustering is a distance-based clustering and requires the number of clusters beforehand. However, it is often difficult to know the exact number of clusters (i.e., labelled neurons) in the Tetbow sample. Mean-shift clustering is a density-based clustering and requires a density kernel beforehand. However, the density of the fluorescence signals (i.e., the total length of the neurites) is not necessarily equal among neurons in the Tetbow sample.

What we want to do in the QDyeFinder is to classify the neurite fragments based on their colour hue similarity. We, therefore, developed a new unsupervised clustering algorithm, named dCrawler, in which multi-dimensional vector data are classified based on a threshold distance, *Th(d)* (Fig. 4). In the dCrawler method, we aimed to classify data points into clusters, so that data points within a cluster are all within a defined *Th(d)* from their centroid position.

In the dCrawler, the first data point will be the first cluster. If a new data point is within *Th(d)* from the centroid position of the existing cluster, we included it in that cluster and updated the centroid position. If the data point is separated by >*Th(d)* from the centroids of any existing clusters, we assigned a new cluster to the data point. We repeated this process until all of the datapoints are assigned to clusters (Fig. 4a-f). To avoid a primacy bias, we then re-allocated points to their closest centroid and updated the centroid positions (Fig. 4g-i). Lastly, we merged clusters whose centroids are located within a defined distance (Fig. 4j-l). All the processes were repeated until all the data points are assigned to clusters. To avoid infinite looping, the merging threshold begins to be gradually reduced (*Th(d)**0.99) for each loop after 20 loops. Eventually, we can obtain clusters whose data points are within *Th(d)* from their centroids (Fig. 4l).

Once we have defined an appropriate *Th(d)* value based on experimental data (e.g., small-scale data under similar conditions), we should be able to classify numerous neurite fragments based on the similarity of their colour vectors. Under the appropriate *Th(d)* value, each of the clusters should represent neurites from a single neuron.

Evaluating the performance of QDyeFinder

To evaluate the performance of QDyeFinder, we compared the performance with conventional manual tracing. We used a 100 μm-thick 4-week-old mouse brain sample, in which layer 2/3 neurons were labelled with 7-colour Tetbow. After obtaining 7-channel images with a confocal microscope with a 63x Objective (NA = 1.30), we found 35 neuronal somata expressing at least one of XFPs. To obtain the "ground-truth" data, we manually traced all the neurites (mostly dendrites) from the 35 neuronal somata (Fig. 5a). The traced neurites were then broken into smaller fragments according to the standard procedure in QDyeFinder (Fig. 3b). We examined whether dCrawler with an appropriate *Th(d)* value can accurately classify the neurite fragments for different neurons.

Using manually traced ground truth data, we checked whether the colour hues are consistent across all the neurite fragments. We examined the distribution of colour vectors and found that for most neurons, the distance (*d*) to the mean value of all the neurite fragments belonging to that neuron is less than 0.2 for most of the neurons (Fig. 5b, Extended Data Fig. 5a, b, and Supplementary Fig. 2). UMAP plotting of all the 679 neurite fragments demonstrated clear discrete clusters, each of which represents neurite fragments from the same neuron (Fig. 5c). We next optimized the *Th(d)* value for the dCrawler. We used the F1 score to evaluate correct classification based on the ground truth data. We performed dCrawler with different *Th(d)* values and calculated the median F1 score across neurons. For this particular sample, the *Th(d)* that demonstrated the highest median F1 score (0.971) was a *Th(d)* of 0.2. The dCrawler at *Th(d)* = 0.2 identified 42 clusters (Fig. 5e). A side-by-side comparison of the manually traced neurons (blue) and identified clusters (green) demonstrated high degree of consensus (Fig. 5f, Extended Data Fig. 5c, d, and Supplementary Fig. 3). Thus, the performance of neurite reconstruction with QDyeFinder was overall comparable to manual tracing for this sample. The remaining errors (pseudo-

positives and negatives) are likely due to poor colour hue representation, errors in manual tracing, and/or the birthday problem (Fig. 2f).

Automated reconstruction of dendrites and axons with QDyeFinder

We next tried the QDyeFinder pipeline for an independent brain sample without a ground truth data. Again, layer 2/3 neurons were labelled with 7-colour Tetbow using *in utero* electroporation. We took a fluorescence image spanning a 581.53 x 454.32 x 290.41 μm^3 volume using a 20x objective (NA = 0.75) (Fig. 6a). A total of 290 labelled neuronal somata were found within this volume. In addition, it should contain neurites from many more neurons including those extending from outside this volume. The automatic detection program identified 15,174 neurite fragments (median fragment length, 12.1 μm; interquartile range, 7.9-20.3 μm) (Fig. 6b), many of which should be dendrites. The dCrawler at *Th(d)* = 0.2 identified 302 clusters (Fig. 6b). In many of the clusters, the identified neurite fragments were spatially clustered, suggesting that each cluster corresponds to neurites from one or a few neurons (Fig. 6c, d). We also ran the dCrawler at different *Th(d)*s where the F1 score was above 0.9, (*Th(d)* = 0.13, 0.15, 0.175, 0.225, 0.25, and 0.26). To evaluate the effectiveness of the clustering each cluster was allocated into one of three groups; where a single neuron is visible (Fig.6d, left panels, >90% of fragments seem to belong to a single neuron), where few fragments are visible but no neuron is visible (Fig. 6d, middle panels, <30% of fragments for a neuron seemed to be detected), and finally a cluster where the fragments belong to two or more neurons (Fig. 6d, right panels). The percentage of clearly visible single neuron clusters increases up to the optimized *Th(d)* of 0.2, and then begins to decrease. We sometimes observed occasions where multiple clusters actually represented the same neuron, especially at lower *Th(d)* values (Extended Data Fig. 6).

We next examined whether QDyeFinder can accurately reconstruct axons. Reconstructing long-range projecting axons are more challenging than dendrites, as axons are much longer and thinner. We tested mitral/tufted cells in the olfactory bulb, which project millimetre-long axons to the olfactory cortices. A typical mitral/tufted cell project a single axon within the lateral olfactory tract (LOT) and extends several collaterals towards various cortical regions. AAV-CAG-tTA and AAV-TRE-XFP were locally injected into the olfactory bulb to brightly label a limited number of neurons (<100). Three weeks after the injection, the LOT and olfactory cortices were imaged with confocal microscopy (20x Objective, NA = 0.75) (Fig. 7a). In a pilot trial with a small-scale sample, we compared the results of QDyeFinder and manually traced ground truth and obtained F1 score of 0.955 at *Th(d)* = 0.2 (Extended Data Fig. 7). Then, we tested large-scale images (2629.5 x 1636.4 x 437.3 μm^3). A total of 4230 axonal fragments were automatically detected (median fragment length, 24.1 μm; interquartile range, 14.4-50.5 μm) (Extended Data Fig. 8). We classified the type of the clusters (single neuron, few fragments, and multiple neurons) at varying *Th(d)*s. We found that a *Th(d)* of 0.25 produced the highest number of single neuron clusters (Supplementary Fig. 8c). Therefore, we evaluated the fragments at *Th(d)* = 0.25. A dCrawler at *Th(d)* = 0.25 identified 88 clusters, with 14 clusters that clearly label axons for a single neuron (Fig. 7c, and Extended Data Fig. 8b). Many of the clusters included axons spanning a millimetre scale. Thus, super-multicolour labelling combined with QDyeFinder can be used for the analysis of long-range axonal projection.

Discussion

During the past years, large-scale image acquisition is becoming easier for EM and LM-based connectomics. However, circuit reconstruction is still a laborious and technically challenging. Existing neurite reconstruction pipelines are based on "tracing" of physically continuous structures. Thus, slight damage to the images would have a deleterious impact for successful circuit tracing. The error rates will exponentially increase as the distance of the traced neurites increases, hampering large-scale reconstructions.

In this study, we developed a conceptually new type of neurite reconstruction pipeline based on super-multicolour labelling and QDyeFinder. In this strategy, we identified neurite fragments only based on their colour hue information. In other words, each of the neurite fragments have a unique fluorescent "barcode" [4]. We, therefore, do not need to care about the physical continuity of the neurite fragments. This means that the physical distance does not limit the accuracy of the reconstruction, as in previous methods. We do not even need to take continuous images of neurites as long as the neurons are labelled with unique and consistent colour hues (Extended Data Fig. 9). Moreover, QDyeFinder is fully automated, and excludes any human biases in reconstruction. This is conceptually similar to a DNA barcode-based connectomics, such as MAPseq and BARseq [20, 27]. However, our fluorescent protein-based approach is more useful for morphological analyses in 3D.

With 7 XFPs, we can differentiate 99.9% of neuronal pairs. However, the practical limit of neuronal numbers is ~100 due to the birthday problem (Fig. 2g). For example, clusters frequently contained multiple neurons in Fig. 6, where >290 neurons were labelled. In contrast, a majority of the clusters corresponded to single neurons when <100 neurons were labelled (Fig. 5 and Extended Data Fig. 7). Thus, it is critical to limit the number of labelled neurons to identify majority of neurons with unique colour hues. It is also important to label neurons brightly. To obtain consistent colour hues, it is important to avoid photo-bleaching. Tissue clearing is also important as blue signals scatter more in thick brain samples. Fluorescent proteins are bright and stable in the clearing agent, SeeDB2G [13].

With our QDyeFinder, unsupervised clustering with dCrawler was critical. The appropriate *Th(d)* value should be determined based on the stability of colour hues within a neuron and number of labelled neurons in the sample. dCrawler has unique advantages over existing clustering algorithms (Extended Data Table 1) and should be useful for various kind of high-dimensional data analysis, not only in biology (e.g., cell typing with highly multiplexed *in situ* hybridization and/or antibody staining), but also in other fields.

In the future, we may be able to differentiate more neurons with unique colour hues, if we can utilize more XFPs. Chemical tags are also potentially useful to expand spectral variations [12]. While 7 XFPs are close to the upper limit due to spectral overlap, we may be able to utilize fluorescent lifetime to further differentiate more XFPs [28, 29]. If we can use peptide-based barcodes and detect them by serial antibody staining [30, 31], we should be able to massively increase the number of unique labels [32].

In this study, we utilized super-multicolour imaging and QDyeFinder for neurite identification. In the future, we should be able to use a similar approach for time-lapse imaging. Like neurite reconstruction in 3D, cell tracking is challenging in a single-colour time lapse images. Super-multicolour labelling with QDyeFinder should facilitate more accurate cell tracking. While we ignored spatial information in our QDyeFinder pipeline, we can, of course, consider both spatial and colour hue information for more accurate neurite/cell tracking. Our quantitative approach should be useful for highly multiplexed fluorescence imaging for various kinds of applications.

Acknowledgement

We thank M. Nishihara, T. Ohmine, and The Research Support Center, Research Center for Human Disease Modeling, Kyushu University Graduate School of Medical Sciences, for technical assistance; Elvire Guiot for sharing their application note on Leica HyD; David Gilbert at Randomwire for permission to use an image of Tokyo railway map. This work was supported by Brain/MINDS project (JP20dm0207055 to TI) and iBrain/MINDS project (JP22wm0525012 to TI) from AMED, JST CREST program (JPMJCR2021 to TI), Grants-in-Aids from MEXT (JP16H06456, JP21H00205 and JP21H05696 to TI), JSPS KAKENHI (JP17H06261 and JP21K19355 to TI; JP19K16261 and JP21K06411 to MNL; JP19K06886 to SF; JP21H02140 and JP22K18373 to S.I.), and a grant from the Uehara Memorial Foundation (to TI). D.M. is a predoctoral research fellow (DC1) of JSPS. B.S. is a MEXT scholar for international students.

Author contributions

M.N.L. performed most of the data analysis. S.F. and T.B. performed super-multicolour imaging of brain samples. D.M. and M.N.L developed linearity correction program. B.S. wrote a post-hoc correction program for chromatic aberration in Python. R.S. and S.I. assisted initial phase of the study. T.I. supervised the project. M.N.L, S.F, T.B, and T.I. wrote the manuscript with inputs from all the authors.

METHODS

Plasmids

XFPs were initially selected based on the information in FPbase (https://www.fpbase.org/) [33]. Candidate XFPs were further evaluated based on the brightness and distribution in neurons. pCAG-tTA (Addgene #104102), pAAV-SYN1-tTA (Addgene #104109), pBS-TRE-mTurquoise2-WPRE (Addgene #104103), pAAV-TRE-mTurquoise2-WPRE (Addgene #104110) were described previously [12]. mTagBFP2 [34] was generated from TagBFP (Evrogen). mNeonGreen [35] was obtained from Allele Biotechnology. YPet [36] was amplified by PCR from pCAGGS-RaichuEV-Rac [37]. Plasmids encoding, mAmetrine1.1 [36] (Addgene #18084), mRuby3 [38] (Addgene #74234), and tdKatushka2 [39] (Addgene #30181) were obtained from Addgene. Each XFP gene was PCR-amplified and subcloned into pBS-TRE or pAAV-TRE vector [12]. pBS-TRE-mTagBFP2-WPRE (Addgene #193332), pBS-TRE-mAmetrine1.1-WPRE (Addgene #193333), pBS-TRE- mNeonGreen-WPRE (Addgene #193334), pBS-TRE-YPet-WPRE (Addgene #193335), pBS-TRE-mRuby3-WPRE (Addgene #193336), pBS-TRE-tdKatushka2-WPRE (Addgene #193337), pAAV-CAG-tTA (Addgene #193338), pAAV-FLEX-tTA (Addgene #149363), pAAV-TRE-mTagBFP2-WPRE (Addgene #193339), pAAV-TRE-mAmetrine1.1-WPRE (Addgene #193340), pAAV-TRE-mNeonGreen-WPRE (Addgene #193341), pAAV-TRE-YPet-WPRE (Addgene #193342), pAAV-TRE-mRuby3-WPRE (Addgene #193343), and pAAV-TRE-tdKatushka2-WPRE (Addgene #193344) were generated in this study and are available at Addgene.

Mice

All animal experiments were reviewed and approved by the Institutional Animal Care and Use Committee of Kyushu University. ICR mice (Japan SLC, RRID: MGI: 5652524) were used for *in utero* electroporation. C57BL/6N mice (Japan SLC, RRID: MGI: 5658686) and mitral/tufted cell-specific Pcdh21-Cre [40] mice were used for used for AAV experiments (8-13 week-old male).

In vitro experiments (HEK cells and spectrum data)

HEK293T cells were cultured in high-glucose DMEM (044-29765, FUJIFILM-Wako) with 10% FBS, and 1% penicillin/streptomycin (FUJIFILM -Wako) under the humidified conditions in 95% air and 5% CO2 at 37°C. For spectral measurements, pCAG-tTA2 (0.35 ug) and one of pBS-TRE-XFP-WPRE (0.9 ug) vectors were transfected to 50-80% confluent HEK293T cells in 35-mm dish using PEI-MAX (25 mM, 5 μL/dish; Polysciences, Inc.). Twenty-four hours after transfection, cells were washed twice with 1 mL of PBS, and collected with 1 mL of PBS. Cell suspensions were transferred into a glass cuvette. Excitation and emission spectra were quantified using a fluorescence spectrophotometer (F2700, Hitachi). For each XFP, spectra were measured 5 times in 0.5 nm wavelength increments and averaged. Excitation (ex) and emission (em) wavelengths to determine the spectral curves (ex, em) were as follows (in nm): mTagBFP2 (400, 460), mTurquoise2 (430, 505), mAmetrine1.1 (400, 535), mNeonGreen (465, 540), YPet (490, 550), mRuby3 (530, 610), tdKatushka2 (550, 650). To obtain reference images for unmixing, single colour labelled cells were cultured on a poly-D-lysine coated 35-mm glass-bottom dish (MatTek). Twenty-four hours after transfection, cells were fixed with 4% paraformaldehyde, washed twice with PBS, and treated with SeeDB2G solution [13].

In utero electroporation

In utero electroporation was performed as described previously [12]. To label cortical layer 2/3 neurons in S1, 1-2 μL of plasmid solutions (0.1 μg/ μL of pCAG-tTA and 0.1 μg/ μL of pBS-TRE-XFP-WPRE each) were injected into the lateral ventricle at E15 and electric pulses (a single 10-ms poration pulse at 72 V, followed by five 50-ms driving pulses at 42 V with 950-ms intervals) were delivered toward the medio-lateral axis of the brain with forceps-type electrodes (LF650P5, BEX) and an electroporator (CUY21EX, BEX).

AAV production

AAV vectors (serotype DJ) were generated using the pHelper (AAVpro Helper-free system, Takara), pAAV-DJ (Cell Biolabs), and the AAVpro 293 T cell line (#632273, Takara) following the manufacturers' instructions. AAV vectors were purified using the AAVpro Purification Kit All Serotypes (#6666, Takara). Viral titers were measured using AAVpro Titration Kit (#6233, Takara) or THUNDERBIRD SYBR qPCR Mix (QPS-201, TOYOBO) with StepOnePlus system (ThermoFisher) or QuantStudio3 real-time PCR system (Applied Biosystems).

AAV injections into the olfactory bulb

To infect the Tetbow AAV vectors, C57BL/6N mice (Extended Data Fig. 9) and Pcdh21-Cre mice [40] (Fig. 7 and Extended Data Fig. 7-8) at age 8-13W were used. Mice were anaesthetised with i.p. injection of ketamine (100 mg/kg) and xylazine (10 mg/kg). The hair

between the mouse's head and the ears was removed, then mouse was fixed onto a stereotaxic frame (Stoelting). The scalp and underlying connective tissue was then removed. Skull over the olfactory bulb was drilled. Injection depth was ~0.1 mm. Then, the virus was slowly injected at a rate of 2.3 nL every 6 seconds for 2 minutes (total 46 nL) using the nanoject II system and glass capillaries (#3-00-203-G/XL, Drummond). The concentration of the injected virus cocktail was 4×10^9 gc/mL for AAV2/1-FLEX-tTA2 and 1.25×10^9 gc/mL each for AAVDJ-TRE-XFP-WPRE. Before and after the injection, the needle was kept in place for 5 minutes. The hole on the skull was covered with superglue and the exposed skull was then covered with dental cement. Post-surgery, the body of the mouse was kept warm to facilitate recovery. As toxic effects of prolonged XFP expression began to be observed after 4 weeks post injection, mice were sacrificed 3-4 weeks after virus injection [12].

Sample preparation and tissue clearing with SeeDB2G

To obtain brain tissue, mice were intraperitoneally injected with an overdose of pentobarbital (P0776, TCI) in PBS to produce deep anaesthesia, followed by an intracardiac perfusion with a 25 mL PBS wash followed by 25mL of 4% PFA in PBS. Excised brain samples were then fixed with 4% paraformaldehyde in PBS at 4°C overnight. Brains were then embedded in 4% agarose (ThermoFisher, #16520-100). Cortical samples were cut into 120- or 320-μm-thick slices with a microslicer (PRO7N, Dosaka EM), and cleared with the SeeDB2G protocol [13]. Cleared cortical samples were then mounted in SeeDB2G (Omnipaque 350, Sankyo) on a glass slide using a 0.1 or 0.3 μm-thick silicone rubber sheet (AS ONE, #6-9085-12 or #6-9085-14, Togawa rubber) and glass coverslips (Marienfeld, No. 1.5H, #0109030091) as described previously [41].

To analyse long-rage axonal projections of M/T cells, a brain hemisphere was dissected, and the dorsal part and subcortical matter was trimmed away with forceps and a scalpel. The remaining part, containing all of the olfactory cortical areas, was flattened with a 1 mm spacer, and fixed with 4% PFA in PBS overnight at room temperature on a rocker [12]. Then, the sample was treated with ScaleCUBIC-1 [42] (25% (wt/wt) urea (#219–00175, Wako), 25% (wt/wt) N,N,N',N'-tetrakis(2-hydroxypropyl)ethylenediamine (#T0781, TCI), and 15% (wt/wt) Triton X-100 (#12967–45, Nacalai-tesque) in H2O) for 24 hr to remove lipids from the lateral olfactory tract, washed with PBS, and then cleared with SeeDB2G as described previously [13, 41].

Confocal microscopy

Samples cleared with SeeDB2G were mounted on glass slides with 100 or 300 μm-thick silicone rubber spacer. Samples were imaged with an inverted confocal microscope, SP8 TCS (Leica) with HyD detectors. 20x (HC PL APO 20x/0.75 IMM CORR CS2) and 63x (HCX PL APO 63x/1.30 GLYC CORR 37°C) objective lenses were used. Type G glycerol immersion (ThermoFisher, Cat#15336741) were used. XFPs were excited at 405, 488, or 552 nm lasers and emission signals were dispersed by a diffraction gating as described in legends to Fig. 1c. Pinhole size was set at 1 A.U. Images were acquired under "standard mode" and at 16-bit. Linearity was even worse under "photon counting mode". At both conditions, linearity was poor when recorded at 16-bit [18, 19], and linearity correction was needed as described below.

Linearity correction for fluorescence intensity acquired with Leica HyD detectors

Measuring reference data and calculating the coefficients

HEK293T cells were transfected with mNeonGreen, then following fixation they were imaged with an inverted confocal microscope with the laser power increasing for 0.2 to 3% with 0.2% intervals (Extended Data Fig. 1a, b, SP8 TCS with HyD detectors, Leica). Laser power was linearly controlled by ATOF. The intensity values for each pixel were then recorded and the values from 0.2% to 1% were used to calculate a linear trend unique to each pixel (Extended Data Fig. 1c). This was then used to create a predicted value for each original intensity value which can then be used to create a fit to the equation below (Extended Data Fig. 1d).

$$y = ax + (b \times e^{cx}) - b$$

In our microscope, a = 0.9838, b = 1.1044, and c = 0.001. As we can see in Extended Data Fig. 1b, values above 7,000 were almost saturated and uncorrectable (Extended Data Fig 1d-f). We, therefore, discarded pixels above 7,000 (assigned "not a number"). Pixels below 7,000 were transformed to produce a corrected image. The MATLAB code for the linearity correction is available at Github (https://github.com/mleiwe/HyD_NonLinearCorrection).

Evaluation of non-linearity corrections

For successful linear unmixing, it is important to ensure that the ratios between channels are consistent across various intensity ranges. We, therefore, evaluated the consistency of the ratio (Ch4 / Ch4 + Ch5) using mNeonGreen. ROIs for HEK293T cells were determined using Cellpose 2.0 (https://www.cellpose.org/) [43]. This was used to exclude background voxels from our ratio calculations. (Extended Data Fig 1g-i).

Soma detection for brain samples

All neurite tracing and soma detection was performed in Nerurolucida 360 (MBF Biosciences). For Soma detection, somas were initially detected with the automatic algorithm, followed by manual guided detection of the remaining soma.

Manual neurite tracing for ground truth

Neurolucida 360 (MBF Biosciences) was used for manual neurite tracing. For the creation of ground truth dendrite data (Fig. 5a), fully manual tracing was performed on the 63x images containing all of the channels. This enabled the accurate grouping of neurites into sets. For the manual tracing of 20x axon images (Extended Data Fig. 7a), user-guided tracing was performed (with directional kernels selected as the chosen method).

Automatic detection of neurite fragments with Neurolucida 360

For fully automated tracing of neurites, each channel was individually normalized to its maximum, and then the maximum value was taken for each voxel to create a single channel volumetric image. This was then loaded into Neurolucida360 where firstly, the somata were auto detected, adjusting the parameters to ensure all soma were labelled (with remaining soma manually detected). Then, a two-stage auto-tracing procedure was used. First, a rayburst crawl was implemented to detect bright and large neurites, then a directional kernel algorithm was implemented to detect finer less bright neurites (seed density: dense; seed sensitivity: 80; refine filter: 2; trace sensitivity: 70; connect branches and remove traces shorter than… options: de-selected, for both tracing algorithms). Files were then saved as an xml file for export to our MATLAB analysis pipeline. To correct for errors where all

Neurolucida algorithms selected the edge rather than centre of the neurite a custom written MATLAB code was written to move the points to the centre of the neurite.

Unmixing of overlapping fluorescence signals

Reference data was acquired with HEK293T cells expressing each of XFPs and cleared with SeeDB2G. mTagBFP2, mTurquoise2, and mAmetrine1.1 were excited at 405 nm and fluorescence at 410-468 nm (Ch1), 468-505 nm (Ch2), and 520-600 nm (Ch3) were acquired. mNeonGreen and YPet were excited at 488 nm and fluorescence at 495-525 nm (Ch4) and 525-555 nm (Ch5) were acquired. mRuby3 and tdKatushka2 were excited at 552 nm and fluorescence at 575-600 nm (Ch6) and 615-755 nm (Ch7) were acquired. Linearity correction was performed as described above. Based on the ratios across channels, linear unmixing was performed for sample images as described previously [16, 17]. See Supplementary Fig. 2 for more details. Images acquired with 20x and 63x objective lenses were processed with reference data with 20x and 63x, respectively. The MATLAB code for the linear unmixing is available at Github (https://github.com/mleiwe/LinearUnmixing).

Post-hoc correction of chromatic aberration

Correction of chromatic aberration has been described previously [26]. MATLAB and Python codes are available at Github (https://github.com/mleiwe/ChromaticAberrationCorrection). Our program can correct non-uniform chromatic aberrations in cleared tissues *post hoc*.

Extracting colour vectors from neurite fragments

Fluorescence signals were extracted from the Neurolucida 360 traces using custom-built MATLAB codes. The putative fragments then went through a quality control pipeline (Extended Data Fig. 4) as follows. Firstly, traces were split into fragments at all branch points. Secondly, the brightness of each channel was evaluated by calculating the signal to noise ratio for the trace voxels compared to the background (non-traced) voxels. Each channel can be assessed manually or automatically where a minimum signal to noise ratio of 3 was required for a channel to be included. Thirdly, a minimum length of a fragment was calculated (or manually inputted) to remove any short fragments that may have a large degree of colour variability. Fourthly, a minimum brightness was calculated (or manually inputted) in order to prevent analysis of any dim fragments which will have proportionally inaccurate vector normalised values. Finally, fragments where the colour changes significantly ($d > 0.3$) were split at the point of colour change. This occurred often when Neurolucida automatic tracing was performed as it does not use colour information for the tracing. Following these quality control steps, the mean raw intensity values of each fragment was obtained. Then, the median background of each channel was subtracted, and then normalized to the maximum per channel. The resulting values were then vector-normalized to obtain colour vectors.

dCrawler

Clustering was performed from a matrix containing the vector normalised colour values, with the colour vector weighted by the magnitude for the centroid calculations. See Fig. 4 and Supplementary Fig. 1 for more details. The MATLAB code for dCrawler is available at Github (https://github.com/mleiwe/dCrawler).

Calculation of optimum threshold distance

The optimum threshold distance (*Th(d)*) was calculated by using manually traced neurons from Neurolucida 360. The traces were processed the same as the automatically traced neurons. This created fragments that had a known neuron identity as well as a cluster identity. We determined that the correct cluster was the cluster that had the most fragments from the same neuron. This leads us to classify all fragments as true positive (correct cluster and correct neuron), false positive (correct cluster, different neuron), false negative (different cluster, correct neuron), and true negative (different cluster, different neuron). From there an F1 score can be created for each individual neuron. These F1 scores were calculated for each neuron for a range of *Th(d)* from 0.05 to 1. The *Th(d)* with the highest median F1 score was considered optimum.

Modelling and synthetic data

Generation of synthetic data for Tetbow-labelled cells

The generation of N-dimensional colour vectors for "cells" was an extension of the modelling performed in our previous study [12]. Briefly a Poisson probability distribution function was created for a range of copy numbers (average 0, 0.1, 0.2, 0.5, 1, 2, 4, 8 copies / colour / cell) to calculate the probability of up to 50 XFP copies being expressed per cell. This was then fitted to the number of "cells" specified for each dimension, with the order of the expression being shuffled for each channel to simulate the stochastic nature of transfection. The data was then vector normalised to place it into standard colour space (colour vectors).

Percent discriminable

This was performed as has been described in our previous study [12]. Discriminability (where $d > Th(d)$) was tested with 10,000 cells for between 1 – 7 XFPs.

Percent unique

To measure the number of "cells" that had a unique colour, we performed Monte-Carlo simulations (n = 200), by generating simulated colours in N dimensions, with a specified number of cells. "Cells" were classed as unique if they had no other cells within the threshold distance, *Th(d)*. The percent of cells that were unique within each simulation was recorded and the mean and standard deviation were determined. All analysis was performed on MATLAB and are available on GitHub (https://github.com/mleiwe/QDyeFinder)

Data and code availability

All of the image data acquired in this study will be deposited to SSBD:repository (https://ssbd.riken.jp/repository/xxx).

Post-hoc chromatic aberration correction codes (both MATLAB and Python) are available at Github (https://github.com/mleiwe/ChromaticAberrationCorrection).

Linearity correction program for HyD detectors is available at Github (https://github.com/mleiwe/HyD_NonLinearCorrection).

Linear unmixing code is available at Github (https://github.com/mleiwe/LinearUnmixing).

dCrawler written in MATLAB is available at Github (https://github.com/mleiwe/dCrawler).

QDyeFinder written in MATLAB as well as test data is available in Github (https://github.com/mleiwe/QDyeFinder).

Additional resources and protocols are available in SeeDB Resources (https://sites.google.com/site/seedbresources/).

Requests for additional data should be directed to and will be fulfilled on reasonable request by the Lead Contact, Takeshi Imai (imai.takeshi.457@m.kyushu-u.ac.jp).

REFERENCES

1. Lichtman, J.W. & Denk, W. The Big and the Small: Challenges of Imaging the Brain's Circuits. *Science* **334**, 618-623 (2011).
2. Helmstaedter, M. Cellular-resolution connectomics: challenges of dense neural circuit reconstruction. *Nat Methods* **10**, 501-507 (2013).
3. Shapson-Coe, A. *et al.* A connectomic study of a petascale fragment of human cerebral cortex. *bioRxiv*, 2021.2005.2029.446289 (2021).
4. Bae, J.A. *et al.* Functional connectomics spanning multiple areas of mouse visual cortex. *bioRxiv*, 2021.2007.2028.454025 (2021).
5. Oh, S.W. *et al.* A mesoscale connectome of the mouse brain. *Nature* **508**, 207-+ (2014).
6. Winnubst, J. *et al.* Reconstruction of 1,000 Projection Neurons Reveals New Cell Types and Organization of Long-Range Connectivity in the Mouse Brain. *Cell* **179**, 268-+ (2019).
7. Gong, H. *et al.* High-throughput dual-colour precision imaging for brain-wide connectome with cytoarchitectonic landmarks at the cellular level. *Nature Communications* **7** (2016).
8. Peng, H.C. *et al.* Morphological diversity of single neurons in molecularly defined cell types. *Nature* **598**, 174-+ (2021).
9. Xu, F. *et al.* High-throughput mapping of a whole rhesus monkey brain at micrometer resolution. *Nat Biotechnol* **39**, 1521-+ (2021).
10. Cai, D., Cohen, K.B., Luo, T., Lichtman, J.W. & Sanes, J.R. Improved tools for the Brainbow toolbox. *Nat Methods* **10**, 540-+ (2013).
11. Livet, J. *et al.* Transgenic strategies for combinatorial expression of fluorescent proteins in the nervous system. *Nature* **450**, 56-+ (2007).
12. Sakaguchi, R., Leiwe, M.N. & Imai, T. Bright multicolor labeling of neuronal circuits with fluorescent proteins and chemical tags. *Elife* **7** (2018).
13. Ke, M.T. *et al.* Super-Resolution Mapping of Neuronal Circuitry With an Index-Optimized Clearing Agent. *Cell Rep* **14**, 2718-2732 (2016).
14. Xiong, F.Z., Obholzer, N.D., Noche, R.R. & Megason, S.G. Multibow: Digital Spectral Barcodes for Cell Tracing. *PLoS One* **10** (2015).
15. Veling, M.W. *et al.* Identification of Neuronal Lineages in the Drosophila Peripheral Nervous System with a "Digital" Multi-spectral Lineage Tracing System. *Cell Rep* **29**, 3303-+ (2019).
16. Zimmermann, T., Rietdorf, J. & Pepperkok, R. Spectral imaging and its applications in live cell microscopy. *FEBS Lett* **546**, 87-92 (2003).
17. Dickinson, M.E., Bearman, G., Tille, S., Lansford, R. & Fraser, S.E. Multi-spectral imaging and linear unmixing add a whole new dimension to laser scanning fluorescence microscopy. *Biotechniques* **31**, 1272-+ (2001).
18. Borlinghaus, R.T. Sensors and measuring techniques in confocal microscopy. *Technological Readings* (2015).
19. Guiot, E. *Application note: How to obtain the best from SP5/SP8 confocal microscopes using HyD*. (igbmc, 2017).
20. Kebschull, J.M. *et al.* High-Throughput Mapping of Single-Neuron Projections by Sequencing of Barcoded RNA. *Neuron* **91**, 975-987 (2016).

21. Peng, H.C., Ruan, Z.C., Long, F.H., Simpson, J.H. & Myers, E.W. V3D enables real-time 3D visualization and quantitative analysis of large-scale biological image data sets. *Nat Biotechnol* **28**, 348-U375 (2010).
22. Dickstein, D.L. *et al.* Automatic Dendritic Spine Quantification from Confocal Data with Neurolucida 360. *Curr Protoc Neurosci* **77**, 1 27 21-21 27 21 (2016).
23. Longair, M.H., Baker, D.A. & Armstrong, J.D. Simple Neurite Tracer: open source software for reconstruction, visualization and analysis of neuronal processes. *Bioinformatics* **27**, 2453-2454 (2011).
24. Feng, L.Q., Zhao, T. & Kim, J. neuTube 1.0: A New Design for Efficient Neuron Reconstruction Software Based on the SWC Format. *eNeuro* **2** (2015).
25. Roossien, D.H. *et al.* Multispectral tracing in densely labeled mouse brain with nTracer. *Bioinformatics* **35**, 3544-3546 (2019).
26. Leiwe, M.N., Fujimoto, S. & Imai, T. Post hoc Correction of Chromatic Aberrations in Large-Scale Volumetric Images in Confocal Microscopy. *Front Neuroanat* **15** (2021).
27. Chen, X.Y. *et al.* High-Throughput Mapping of Long-Range Neuronal Projection Using In Situ Sequencing. *Cell* **179**, 772-+ (2019).
28. Pepperkok, R., Squire, A., Geley, S. & Bastiaens, P.I.H. Simultaneous detection of multiple green fluorescent proteins in live cells by fluorescence lifetime imaging microscopy. *Current Biology* **9**, 269-272 (1999).
29. Bastiaens, P.I.H. & Squire, A. Fluorescence lifetime imaging microscopy: spatial resolution of biochemical processes in the cell. *Trends Cell Biol* **9**, 48-52 (1999).
30. Wroblewska, A. *et al.* Protein Barcodes Enable High-Dimensional Single-Cell CRISPR Screens. *Cell* **175**, 1141-+ (2018).
31. Viswanathan, S. *et al.* High-performance probes for light and electron microscopy. *Nat Methods* **12**, 568-+ (2015).
32. Hickey, J.W. *et al.* Spatial mapping of protein composition and tissue organization: a primer for multiplexed antibody-based imaging. *Nat Methods* **19**, 284-295 (2022).
33. Lambert, T.J. FPbase: a community-editable fluorescent protein database. *Nat Methods* **16**, 277-278 (2019).
34. Subach, O.M., Cranfill, P.J., Davidson, M.W. & Verkhusha, V.V. An Enhanced Monomeric Blue Fluorescent Protein with the High Chemical Stability of the Chromophore. *PLoS One* **6** (2011).
35. Shaner, N.C. *et al.* A bright monomeric green fluorescent protein derived from Branchiostoma lanceolatum. *Nat Methods* **10**, 407-+ (2013).
36. Ai, H.W., Hazelwood, K.L., Davidson, M.W. & Campbell, R.E. Fluorescent protein FRET pairs for ratiometric imaging of dual biosensors. *Nat Methods* **5**, 401-403 (2008).
37. Komatsu, N. *et al.* Development of an optimized backbone of FRET biosensors for kinases and GTPases. *Mol Biol Cell* **22**, 4647-4656 (2011).
38. Bajar, B.T. *et al.* Improving brightness and photostability of green and red fluorescent proteins for live cell imaging and FRET reporting. *Sci Rep* **6** (2016).
39. Shcherbo, D. *et al.* Far-red fluorescent tags for protein imaging in living tissues. *Biochemical Journal* **418**, 567-574 (2009).
40. Nagai, Y., Sano, H. & Yokoi, M. Transgenic expression of Cre recombinase in mitral/tufted cells of the olfactory bulb. *Genesis* **43**, 12-16 (2005).
41. Ke, M.T. & Imai, T. Optical Clearing and Index Matching of Tissue Samples for High-resolution Fluorescence Imaging Using SeeDB2. *bio-protocol* **8**, e3046 (2018).
42. Susaki, E.A. *et al.* Whole-Brain Imaging with Single-Cell Resolution Using Chemical Cocktails and Computational Analysis. *Cell* **157**, 726-739 (2014).
43. Stringer, C., Wang, T., Michaelos, M. & Pachitariu, M. Cellpose: a generalist algorithm for cellular segmentation. *Nat Methods* **18**, 100-+ (2021).

FIGURE LEGENDS

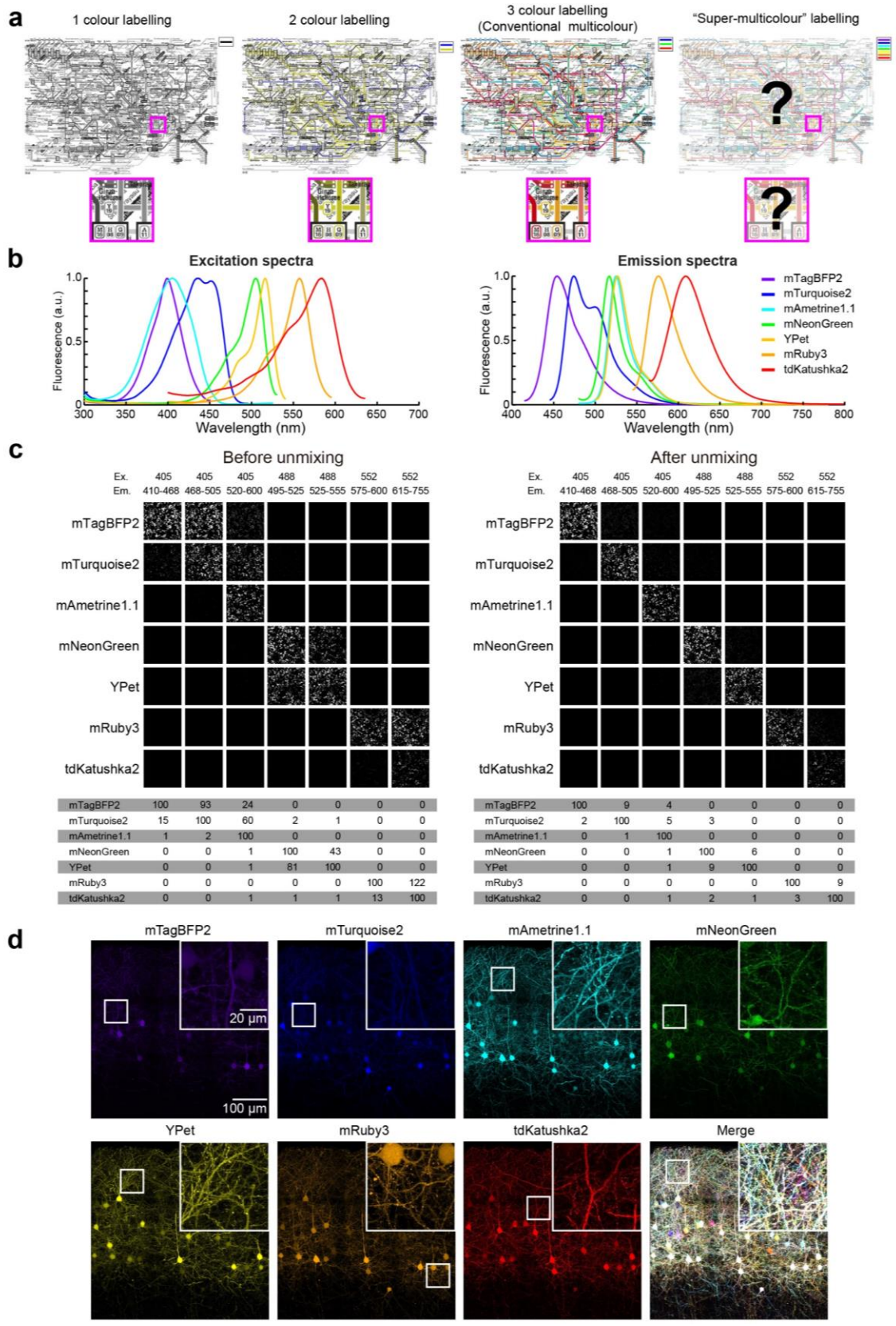

Fig. 1 | 7-colour fluorescence imaging with linear unmixing

a, Cartoons illustrating the concept of super-multicolour fluorescence imaging. Tokyo railway maps shown by the combination of 1-3 colours. Multicolour labelling facilitates identification of different lines. However, using >3 colours is beyond the human visual range.

b, Excitation and emission spectra of our chosen XFPs for 7-colour Tetbow, highlighting the overlap of emission signals between XFPs.

c, 7 XFPs transfected in HEK293T cells before (left panels) and after (right panels) linear unmixing. Reference data for the linear unmixing was acquired from another set of images (Extended Data Fig. 2a). Percentages of normalized intensities are shown below.

d, Layer 2/3 neurons in S1 were labelled with 7-colour Tetbow using *in utero* electroporation. XFP images after linear unmixing are shown. Z-stacked images of 514.57 x 513.49 x 43.48695 μm^3. Inset displays magnified images (white box). Age, P28.

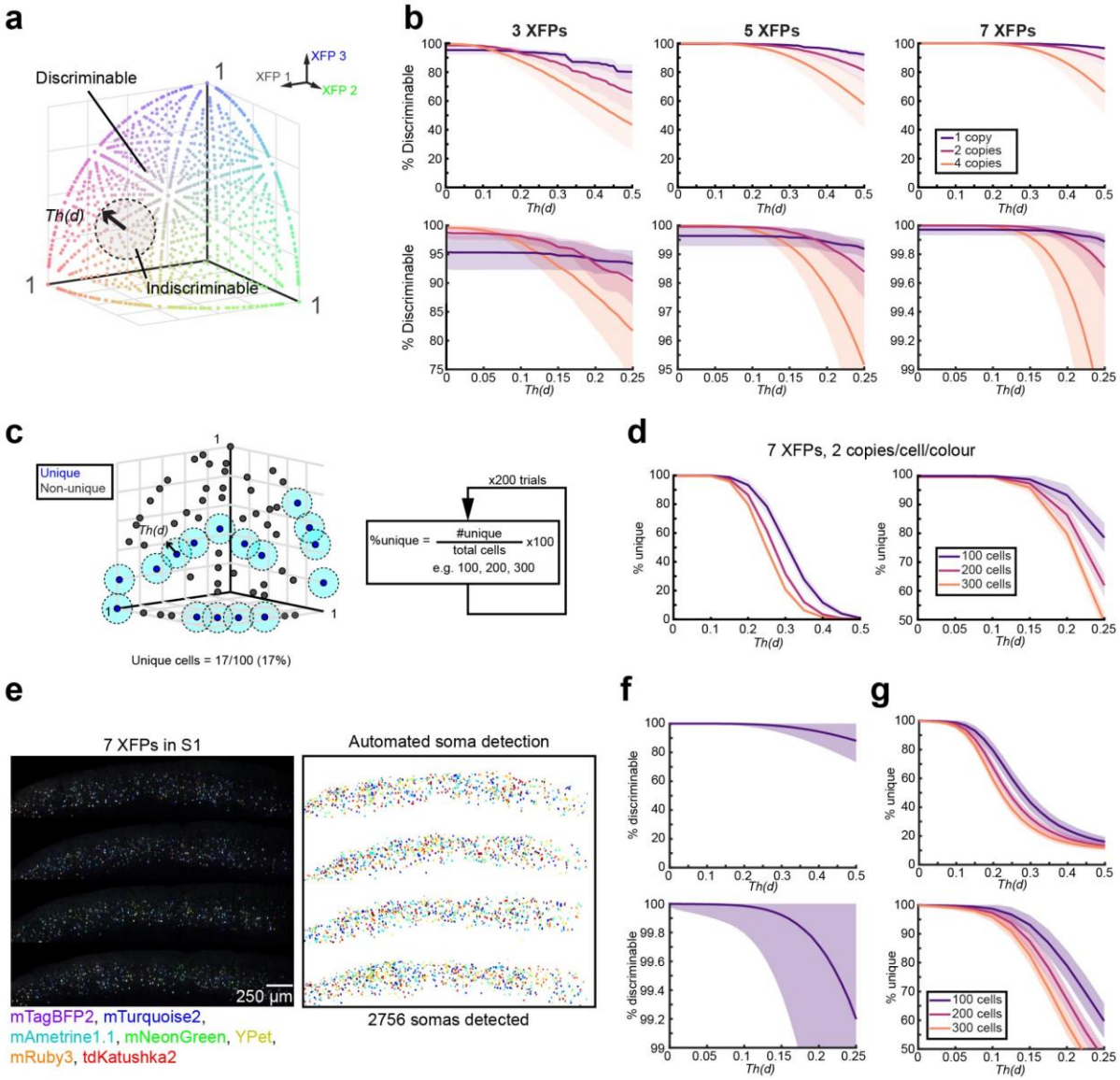

Fig. 2 | 7-colour labelling facilitates unique labelling of more neurons than with 3-colour labelling in Tetbow method.

a, Determining the number of colour vectors discriminable in 3 dimensions. Cartoon illustrating our discrimination analysis. Modelled "cells" within a threshold distance, *Th(d)*, from the chosen cell were considered indiscriminable, and those with a greater distance were considered discriminable.

b, Discrimination analysis of 10,000 modelled cells with up to 7 XFPs. Plots show the mean (bold line) ± 1 standard deviation (shaded areas) for average 1 copy (purple), 2 copies (magenta), and 4 copies (orange) per cell per colour with 3XFPs (left), 5 XFPs (middle), and 7 XFPs (right). Bottom panels are zoomed in insets of the top panels. At all number of colour dimensions 2 copies per colour per cell seemed to be the optimal if the *Th(d)* was between 0.1 and 0.2.

c, Cartoon to measure the uniquely labelled cells. Cells were considered uniquely labelled if there were no neighbouring cells within a specified *Th(d)* (light blue circles). Monte-Carlo simulations (200 per condition) were performed to calculate the percent of unique cells generated at a given number of cells, at varying concentrations, number of XFPs, and varying *Th(d)*s.

d, Modelling results at the optimum conditions (7 XFPs, at average 2 copies per colour per cell). For 100 cells, 93.3% will have a unique colour hue.

e, Evaluation with real data. Four serial sections of S1 labelled with 7-colour Tetbow were imaged. Neurolucida was then used to auto-detect 2031 somata with the mean colour recorded. Z-stacked images of 2677.27 x 2369.32 x 101.9694 μm^3 are shown.

f, Discrimination analysis of somata.

g, Fraction of uniquely labelled cells. 100, 200, or 300 somata were chosen at random (x100 simulations) and the percentage of somata that have a unique colour hue was recorded. Our data suggests that >80% out of 100 cells are uniquely labelled at $Th(d) = 0.2$.

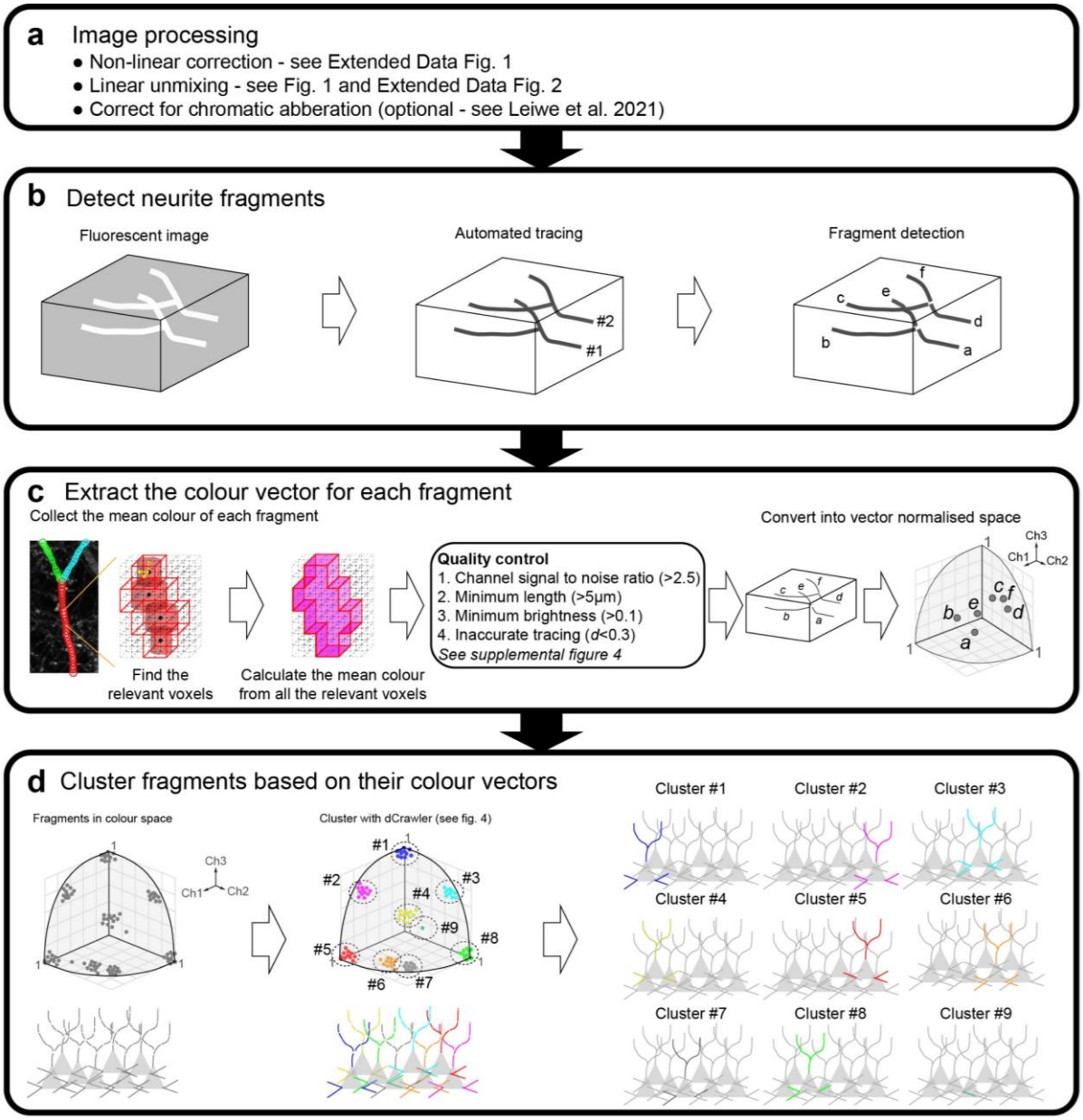

Fig. 3 | QDyeFinder pipeline for automated reconstruction of neurites

a, Image processing. Firstly, the images were non-linearly corrected (see Extended Data Fig. 1), then the images were linearly unmixed (see Fig. 1c, and Extended Data Fig. 2). If axial chromatic aberration correction was necessary, it was performed [26].

b, Neurite detection with Neurolucida 360. Fluorescence images were loaded into Neurolucida 360, to automatically detect neurites using the directional kernels method. However, mistracing frequently occurred in densely labelled images, especially at branch and crossing points. Therefore, detected neurites are split into fragments at branch and crossing points (right). Note that somata were excluded in this step, as they are too bright, and their signals are beyond the linear range.

c, Once the fragments have been detected, the relevant voxels are identified, and the mean pixel intensity is calculated for each channel. After quality control (see Extended Data Fig. 4), fragments are represented in vector normalised space (colour vectors).

d, Colour vectors for the fragments are then clustered based on *Th(d)* with our new clustering algorithm dCrawler (left and middle). Individual clusters can then be plotted to identify neurons from individual fragments (right).

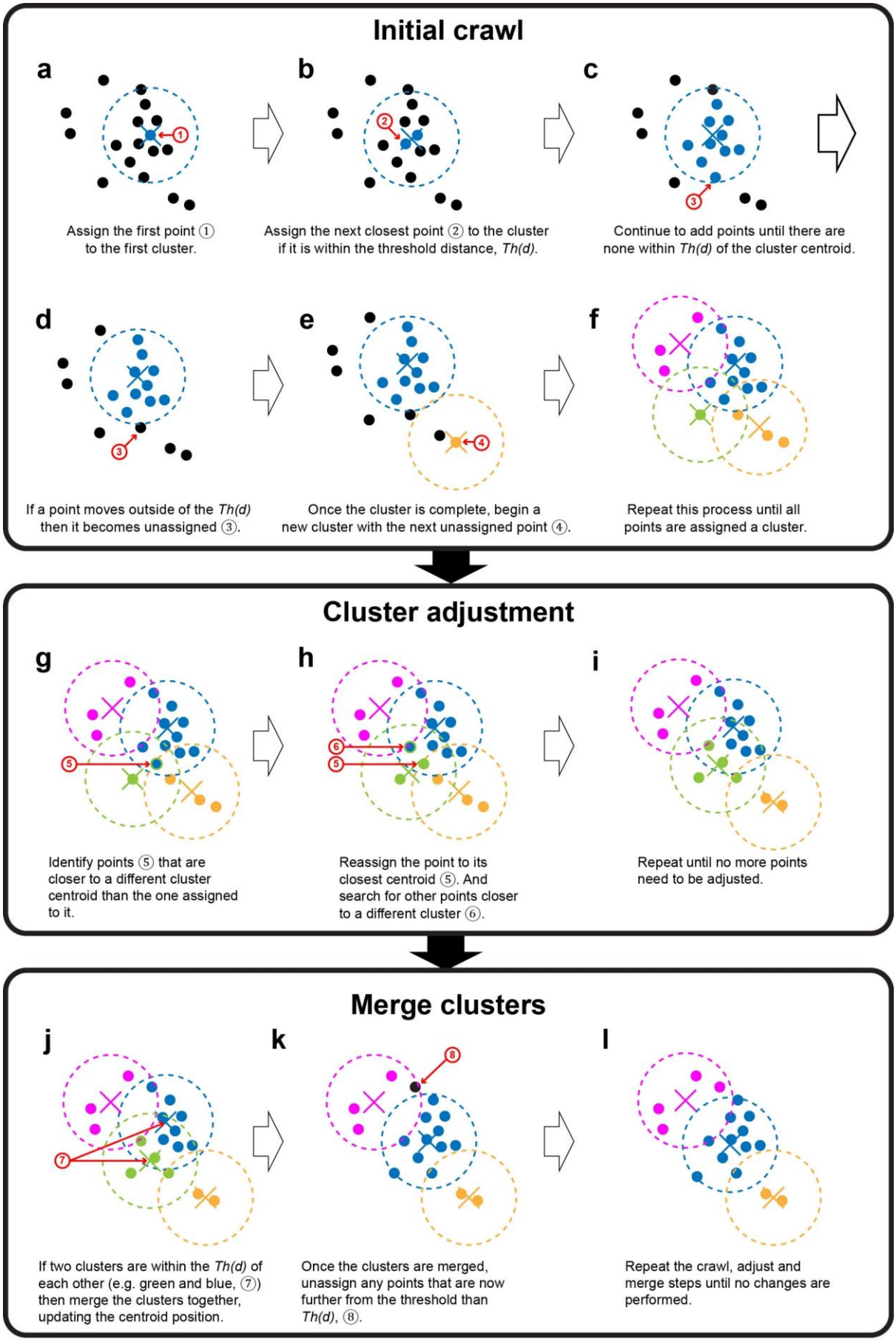

Fig. 4 | Schematic for an unsupervised clustering method, dCrawler

dCrawler has three main steps. The first step is an initial crawl **(a-f)** where a centroid identifies the nearest non labelled point within a specified distance, *Th(d)*, and then updates its position. This continues until all points have an allocated cluster (**f**).

Then, the adjustment phase occurs **(g-i)** where each point is re-allocated to its nearest centroid, and then the centroid positions are updated. This is then repeated until all the points are associated with their closest centroid (**i**).

Next, the merge phase begins **(j-l),** where if any centroids are within *Th(d)* of each other, they are then merged, with the any points that are outside of the cluster being unassigned (e.g. **k**). Finally, the crawl, adjust, and merge steps are repeated until a stable solution is reached.

See Supplementary Fig. 1 and Suppmementary Video 1 for more details.

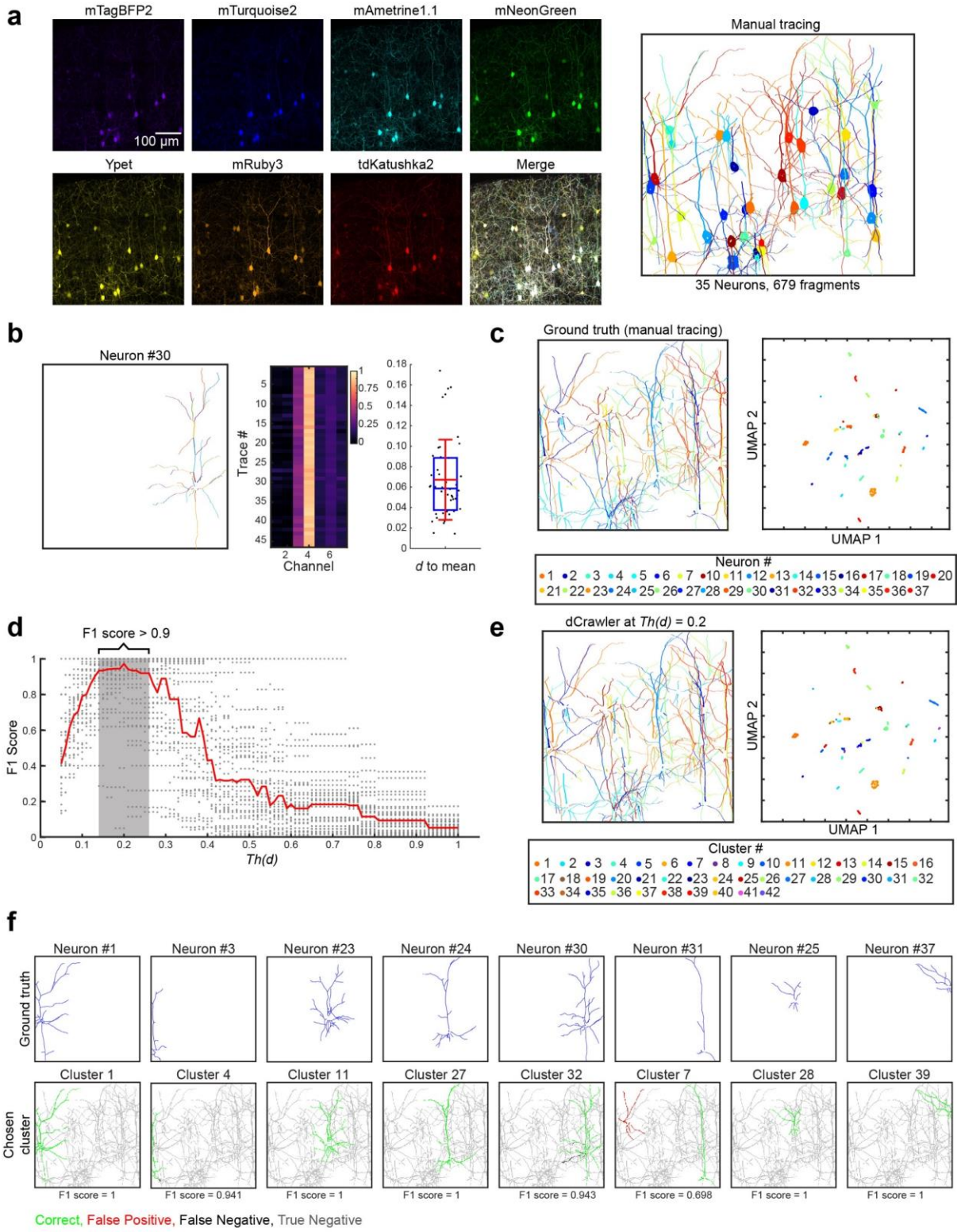

Fig. 5 | Comparison of QDyeFinder versus ground truth with manual tracing

a, L2/3 neurons in S1 were labelled with 7-colour Tetbow via *in utero* electroporation (left). 35 neurons were then manually traced via Neurolucida 360. They were then split into fragments (no branches). Each fragment is represented by a different colour (right). Somata are also highlighted, but were excluded from the analyses. Image taken with a 63x objective lens (NA = 1.30). Z-stacked images of 511.36 x 512.99 x 47.99 μm^3 are shown.

b, A representative example neuron showing the relevant fragments (left), the vector normalised colour vector of each trace (middle), and the Euclidean distance to the mean for the neuron (right). See Supplementary Fig. 2 for all the results.

c, The ground truth of each neuron and their neurite fragments in physical space (left), and in UMAP-reduced colour space (right).

d, The optimum threshold was calculated by running the dCrawler at a *Th(d)* ranging from 0.05 to 1, and calculating F1 score for each neuron at each *Th(d)* (gray dots). The median F1 score for each *Th(d)* is also displayed (red line). The optimum *Th(d)* was calculated to be 0.2.

e, The dCrawler clustering of the neurite fragments at the the optimum *Th(d)*, shown in physical space (left), and in UMAP-reduced colour space (right panel).

f, Representative neurons (ground truth in blue lines, top row) paired to their best cluster. Fragments in both the ground truth and the dCrawler cluster (bottom row) are considered correct (green), those only in the dCrawler cluster are a false positive (red), those in the ground truth only as a false negative (black), and those in neither the ground truth or dCrawler cluster as a true negative (grey). See Supplementary Fig. 3 for all the results.

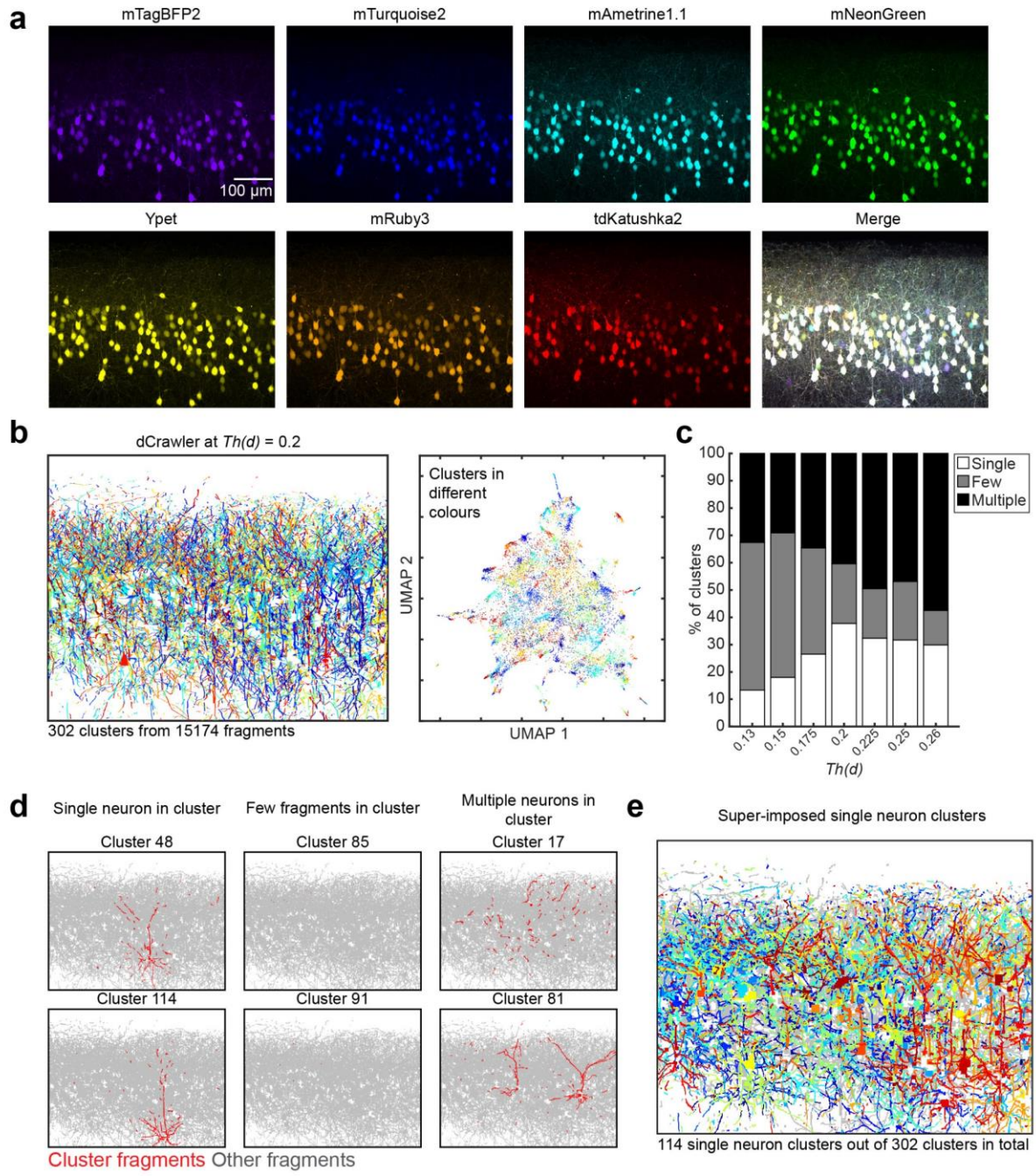

Fig. 6 | Fully automated reconstruction of densely labelled neurons with 7-colour Tetbow in the cerebral cortex

a, L2/3 neurons in S1 labelled with 7-colour Tetbow. Z-stacked images of 581.53 x 454.32 x 290.41 μm^3 are shown. Note that the data are from a representative result from four independent experiments with similar results.

b, 15,174 fragments were then automatically detected using Neurolucida 360 and put through our processing pipeline which detected 302 clusters after clustering at *Th(d)* = 0.2 (left panel). Each fragment is represented by their unique cluster colour in both the fragment plot (left panel) and the UMAP plot (right panel). Colours correspond to each cluster.

c, Classification of dCrawler clusters at a range of *Th(d)*. Clusters were grouped by whether a cluster contained a single neuron, multiple neurons, or few fragments. As with the manually traced data the best results were with the optimum *Th(d)* of 0.2. The optimum *Th(d)* of 0.2 provided the best percentage of single neuron clusters (37.75%).

d, Two representative example clusters are provided for each of the classification groups, fragments belonging to the cluster (red), and the remaining clusters (grey) are shown.

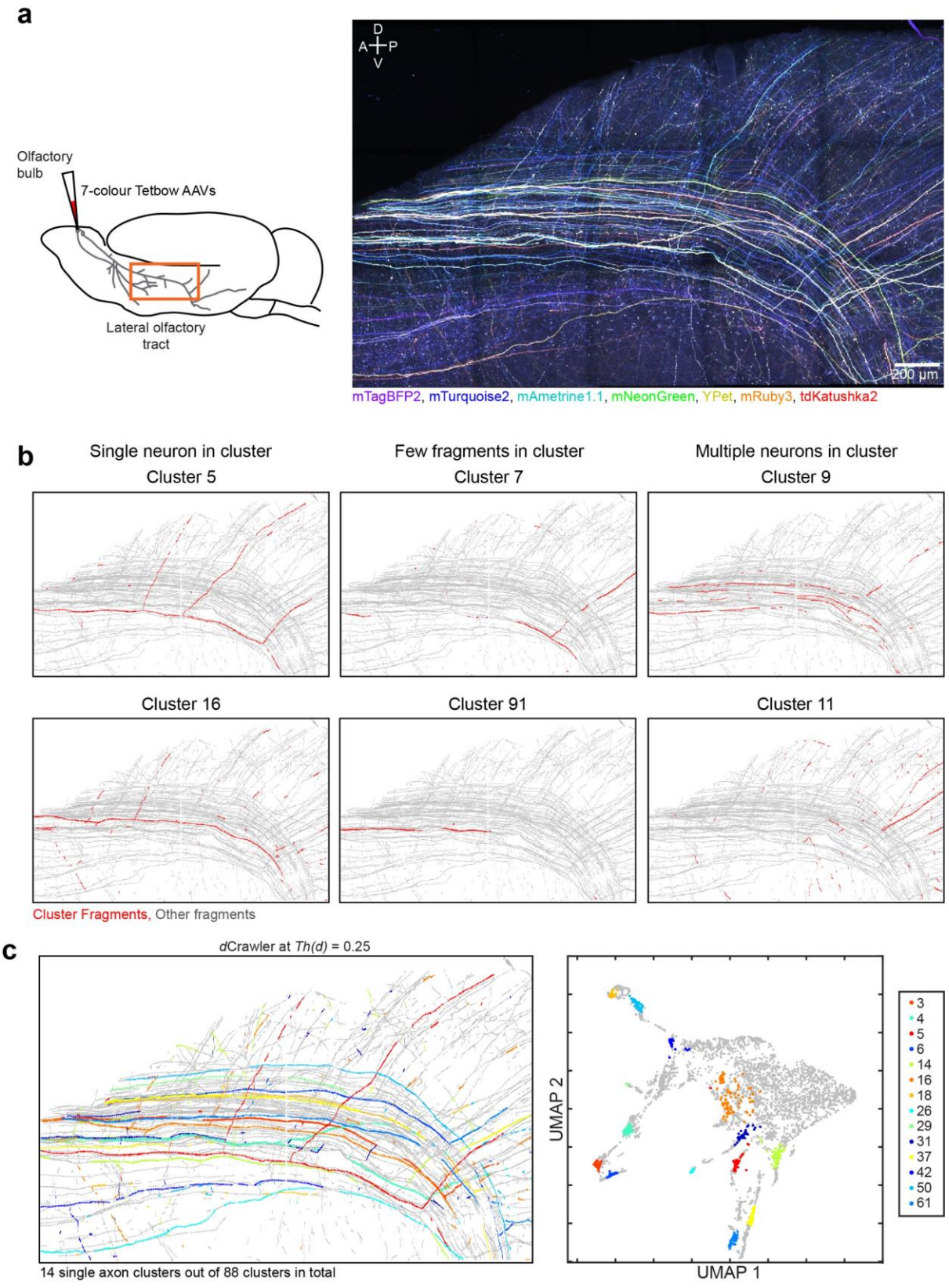

Fig. 7 | Fully automated reconstruction of mitral/tufted cell axons at a millimetre scale

a, A 3 x 5 tiled image (A z-stacked image of 2629.55 x 1636.36 x 437.31 µm^3) of the lateral olfactory tract and olfactory cortex, with mitral and tufted cell axons labelled with 7-colour Tetbow. Mitral/tufted cell-specific Pcdh21-Cre mice and FLEX-tTA AAV was used to label mitral/tufted cells with AAV-TRE-XFP. Images taken with a 20x objective. 7 XFP images

are merged after linear unmixing. Note that the data are from a representative result from four independent experiments with similar results.

b, Representative clusters of the three types after QDyeFinder at *Th(d)* = 0.25. Clusters were either clearly single neuron, containing few fragments, or containing axons from multiple neurons. See supplemental data for more details.

c, All 14 single neuron clusters (left panel) and their positions in UMAP space (right panel). Colours correspond to each cluster. See Extended Data Fig. 8 for individual plots.

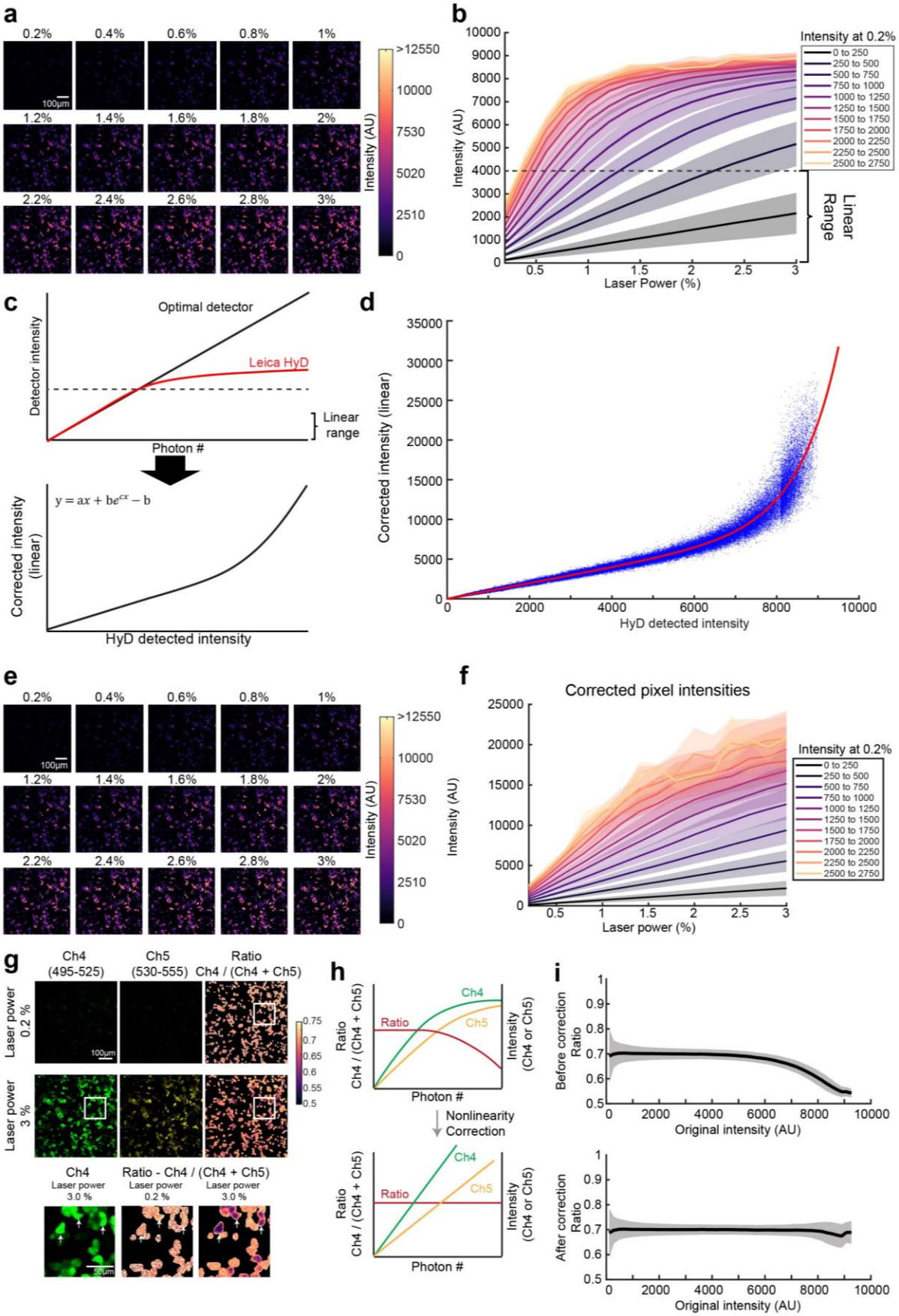

Extended Data Fig. 1 | Linearity correction

a, HEK293T cells transfected with mNeonGreen were cleared with SeeDB2G and imaged at laser powers from 0.2% to 3% to examine the saturation curve of the Leica HyD detectors. Images were acquired under "standard mode" at 16-bit. Laser powers were changed linearly with AOTF.

b, Intensities of pixels as the laser power increases, after the intensity goes beyond 4000 pixels begin to saturate. For the plot, pixels were grouped according to their intensity values at the lowest laser power with the mean (line) ± standard deviation (shaded area) displayed for each group.

c, Top panel, cartoon plot highlighting the difference between an ideal linear detector (black line) compared to the Leica HyD detector which begins to saturate (red line). Bottom panel, the values of our ideal detector can be predicted by extrapolating from the linear range of the HyD detector. An equation can then be fitted and used to convert values from the HyD detector to the linear values.

d, Pixels from the images in **a** were used to determine the equation used to convert intensities. Intensities above 8,000 are still noisy and a poor fit.

e, Corrected images from **a**, showing the improved linearity of the image, especially in the bright range.

f, Corrected intensities of pixels as the laser power increases. Pixels were binned in the same manner as in **b**.

g, Evaluation of non-linearity correction on the ratio of two different fluorescent proteins (Ch4 for mNeonGreen, and Ch5 for YPet). Raw intensity values before unmixing were used to calculate the ratio, Ch4 / (Ch4 + Ch5). Top panel shows the images and ratios at a low laser power (0.2%). Middle panel shows the images and ratios at a high laser power (3%). Bottom panels show the zoomed in areas of the ratiometric image (white box). Note that ratiometric images have an applied mask to remove background signal. White arrows indicate examples where the intensity ratios change with differences in laser power.

h, Schematic cartoon predicting the improvement in the consistency of the ratio values, Ch4 / (Ch4 + Ch5), at all levels of brightness.

i, Changes in ratio, Ch4 / (Ch4 + Ch5), with laser power before and after non-linear correction. Line represents the mean, and the shaded area represents ±1 standard deviation.

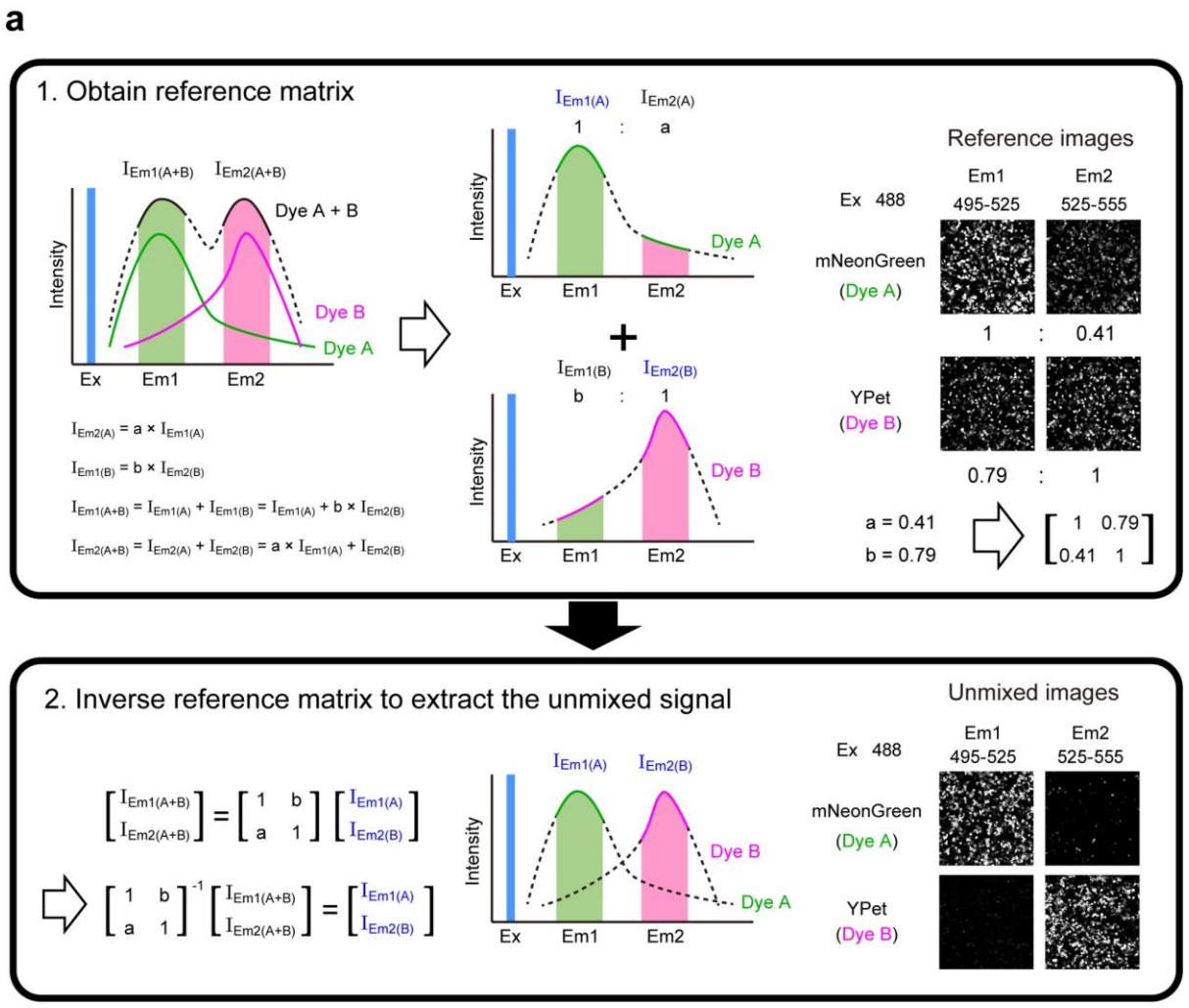

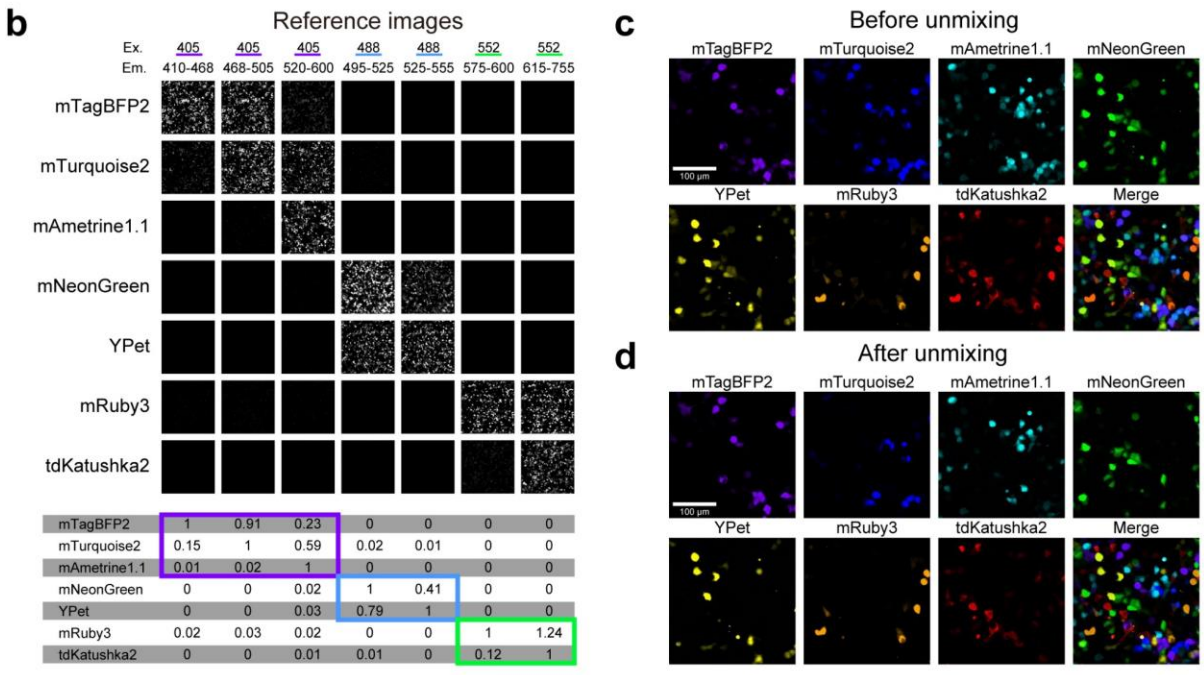

	405 410-468	405 468-505	405 520-600	488 495-525	488 525-555	552 575-600	552 615-755
mTagBFP2	1	0.91	0.23	0	0	0	0
mTurquoise2	0.15	1	0.59	0.02	0.01	0	0
mAmetrine1.1	0.01	0.02	1	0	0	0	0
mNeonGreen	0	0	0.02	1	0.41	0	0
YPet	0	0	0.03	0.79	1	0	0
mRuby3	0.02	0.03	0.02	0	0	1	1.24
tdKatushka2	0	0	0.01	0.01	0	0.12	1

Extended Data Fig. 2 | Linear unmixing separates 7 XFPs.

a, Cartoon to explain the process of linear unmixing. Box 1 left shows the problem when two dyes have spectral overlap. The intensity value recorded by the channel is the sum of intensities of both dye A and dye B. We can then record the reference intensities for both channels recording them as a ratio for each dye (1:a, and b:1 respectively), which can then be expressed as a matrix. The recorded intensity can be expressed as the matrix multiplication of our reference matrix and the intensity signal generated by each dye separately. This means we can rearrange the equation to calculate the intensity signal generated by each dye separately.

b, To generate our reference matrices, HEK293T cells transfected with a single XFP were imaged. There reference values were used to unmix the images in Fig. 1c.

c-d, A mixture of HEK293T cells, each expressing just one type out of 7 XFPs. Images before **(c)** and after **(d)** linear unmixing. We were able to remove spectral overlap so that no cells were double labelled.

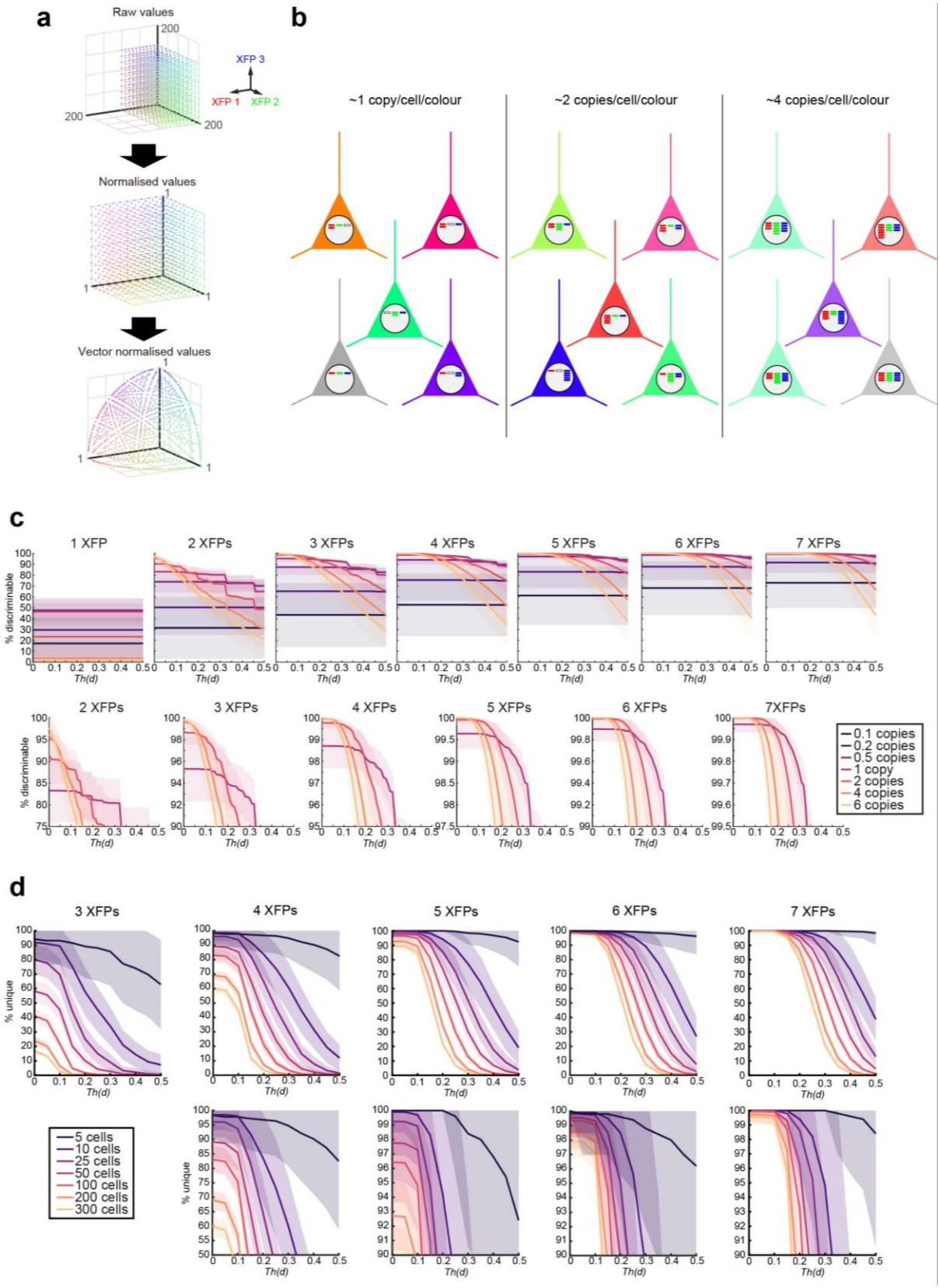

Extended Data Fig. 3 | Additional modelling data.

a, Cartoon showing the conversion of 3-channel fluorescence signals into vector normalised colour vectors. The same scheme was used for N-channel images.

b, Copy number of XFP genes follow Poisson distributions in Tetbow method [12]. Cartoon shows the effect of plasmid/AAV concentrations for 3 XFPs.

c, More detailed investigation of the percent discriminable for 1-7 XFPs at 0.1, 0.2, 0.5, 1, 2, 4, and 6 copies per colour per cell. Top row displays the overall patterns at a *Th(d)* from 0 to 0.5. Bottom row displays a zoomed in version showing the differences between the copy numbers at tighter range.

d, More detailed investigation of the percent of cells unique at 3-7 XFPs when 5, 10, 25, 50, 100, 200, and 300 cells are labelled at 2 copies per cell per colour. Top panels display a broad organisation of pattern for the different number of cells labelled at each number of XFPs. Bottom row contains a zoomed in view of the data in the top row.

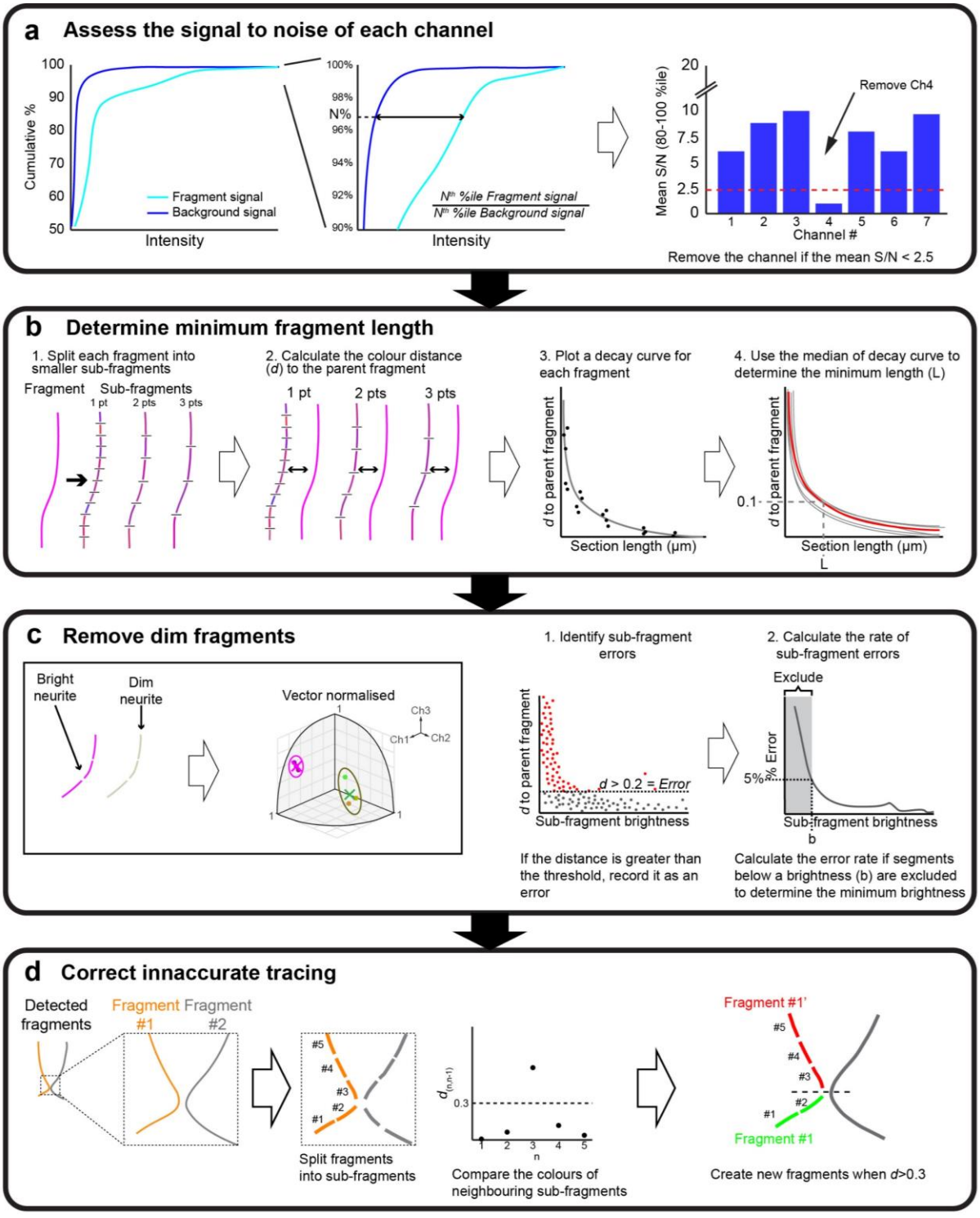

Extended Data Fig. 4 | Quality control for neurite fragment quantifications.

a, Firstly, the overall quality of each channel was assessed by comparing the signal to noise ratio of the voxels labelled in the neurite fragments (cyan) and the background/non-labelled voxels (blue). The mean signal to noise ratio was calculated for each percentile between 80-100 (infinite values excluded). If the mean signal to noise ratio was above 2.5, the channel was retained.

b, Determining the minimum fragment length. Shorter fragments often produce inaccurate colour vectors as they do not have sufficient voxels to produce a stable mean value. To calculate the minimum length of a fragment that produces a stable colour vector, each neurite fragment was split into sub-fragments of varying lengths (leftmost cartoon). The colour distance (*d*) between each sub-fragment and the parent fragment was measured (second left plot), for each fragment a decay curve is fitted (step 3). Finally, the decay curves for each fragment are used to calculate a median decay curve. The minimum length is then calculated at where the curve crosses $d = 0.1$.

c, Dim fragments can also result in inaccurate colour vectors (left panel). Brightness can be measured for a fragment before vector normalisation. To establish the minimum brightness necessary, the fragment was split into sub-fragments each at the minimum distance calculated in **b**. Then the brightness was calculated before vector normalisation. After vector normalization to obtain the colour vectors, distance to the parent fragment (*d*) was measured. If the colour distance was above the specified threshold, it was marked as an error (middle panel). Finally, to calculate the minimum brightness necessary, the error percentage was calculated if sub-fragments less than a particular brightness were excluded. From this line the first brightness value below an error threshold (5%) was selected to be the minimum brightness (b) of a threshold.

d, Another possible error that can emerge from Neurolucida 360 fragment detection. When neurites cross each other, the tracer (automated or manual) can make a wrong decision (left). To correct for this, the fragments were split into small sub-fragments as in **b** and the colour distance (*d*) between neighbouring sub-fragments was measured (middle). If *d* was greater than the specified value (0.3), the fragment was split into two at that point (right).

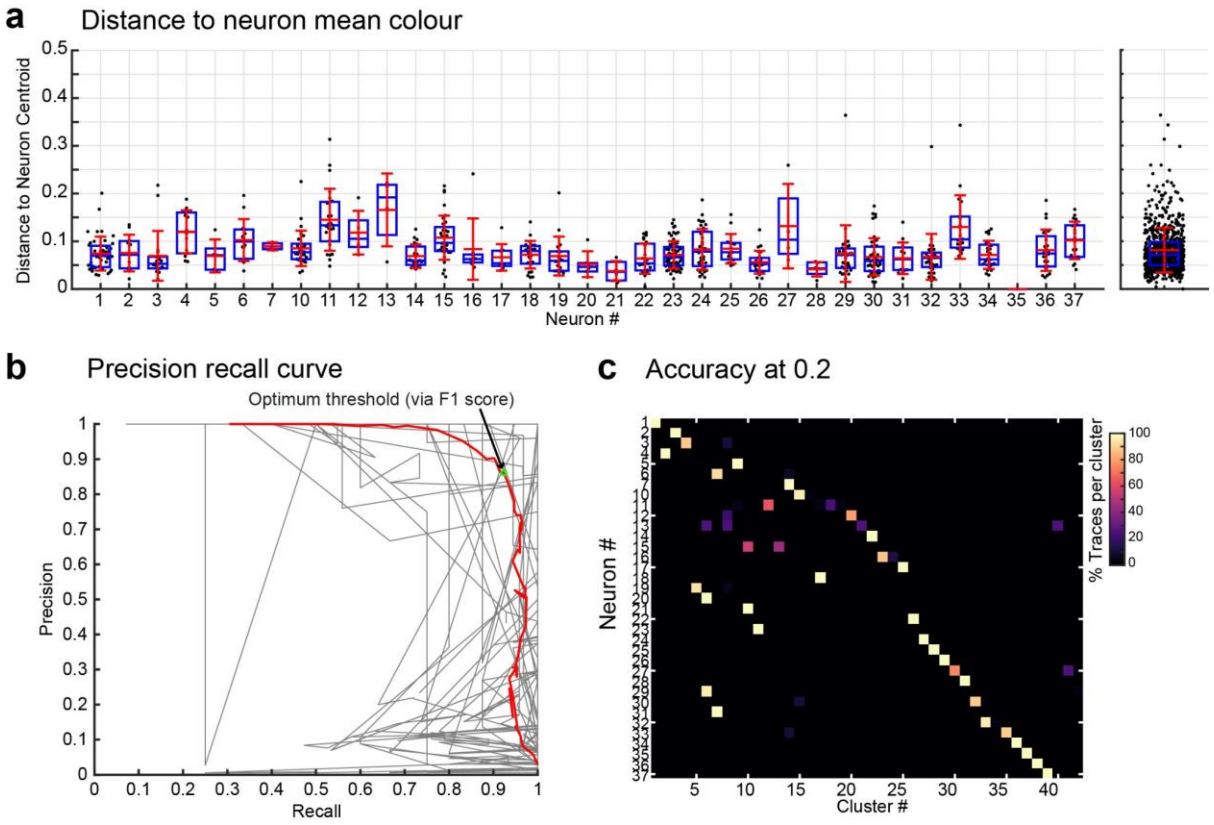

Extended Data Fig. 5 | Optimization of the threshold distance, *Th(d)*.

a, The initial variation of colour vectors per cell. Each fragment is represented by a grey point, mean (red horizontal bar), median (blue horizontal bar), ± 1 standard deviation (red whiskers), and the interquartile range (blue box). Panel on the right shows all the points together.

b, Precision recall curves for each manually traced neuron (grey lines) and the median (red line), with the position of the optimal threshold indicated (green circle). Each point in each curve represents a *Th(d)* ranging from 0.05 to 1. Precision is defined as the number of true positives divided by the sum of the true positives and false positives. Recall is defined as the number of true positives divided by the sum of the true positives and the false negatives.

c, Matrix that displays the percentage contribution of fragments belonging to each cluster (*x*-axis) to the 37 manually traced neurons (*y*-axis). 100% represents the situation where a single cluster includes all the fragments associated with the neuron.

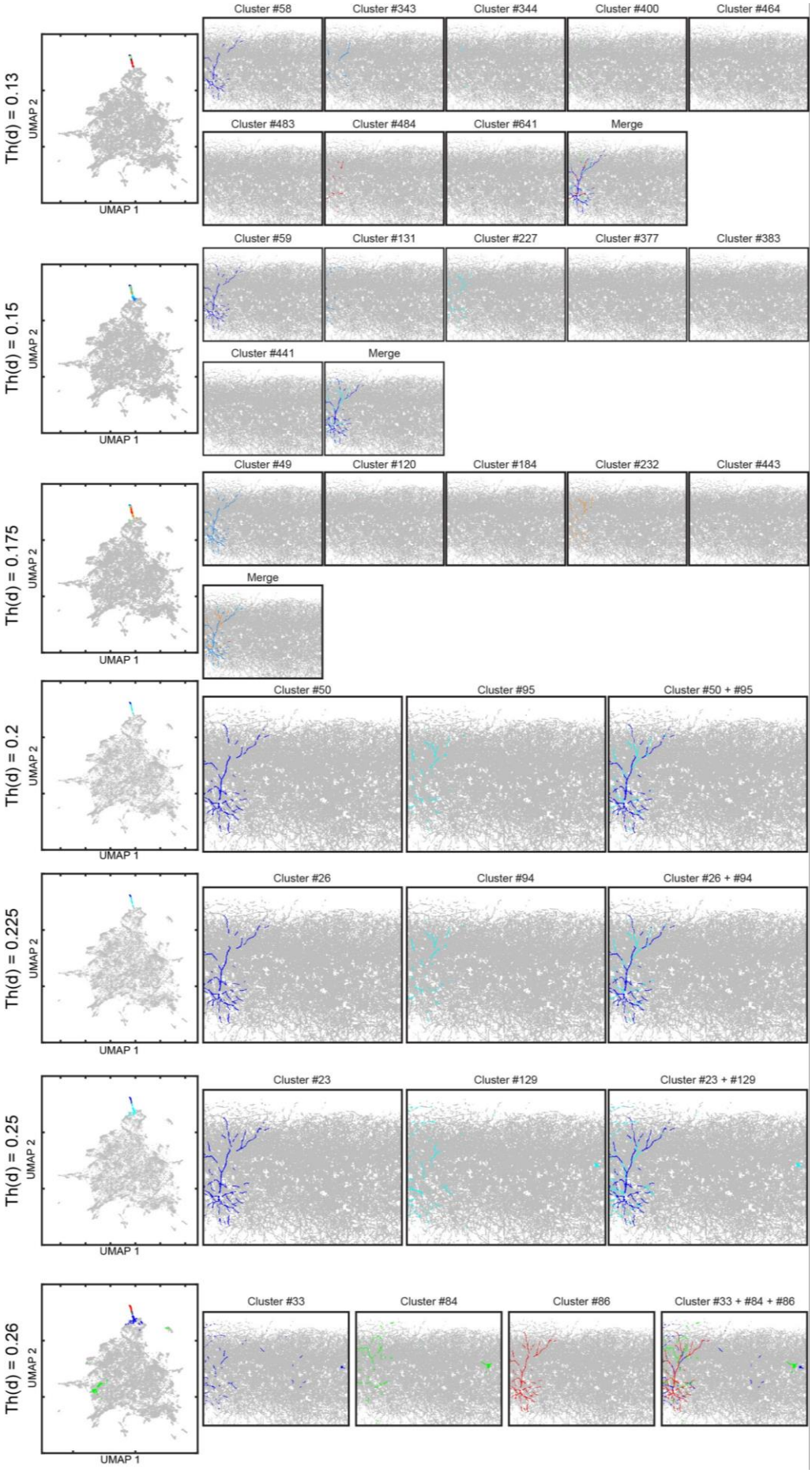

Extended Data Fig. 6 | Investigation into a neuron represented by multiple clusters.

If *Th(d)* is too small, one neuron can split into multiple clusters. By using the UMAP plot we were able to occasionally identify neurons that were spread across multiple clusters. At our optimum threshold of 0.2 we detected that this example neuron contained fragments in clusters 50 and 95 (left panel). Therefore, we plotted all fragments belonging to each cluster separately (middle panels) and combined (right most panel). As we increase the *Th(d)* there are more fragments included within each cluster including false positives that clearly don't belong to the neuron. While as the *Th(d)* decreases there are more clusters associated with the fragments of the neuron. Note that UMAP distance does not necessarily reflect distance in the Euclidean space.

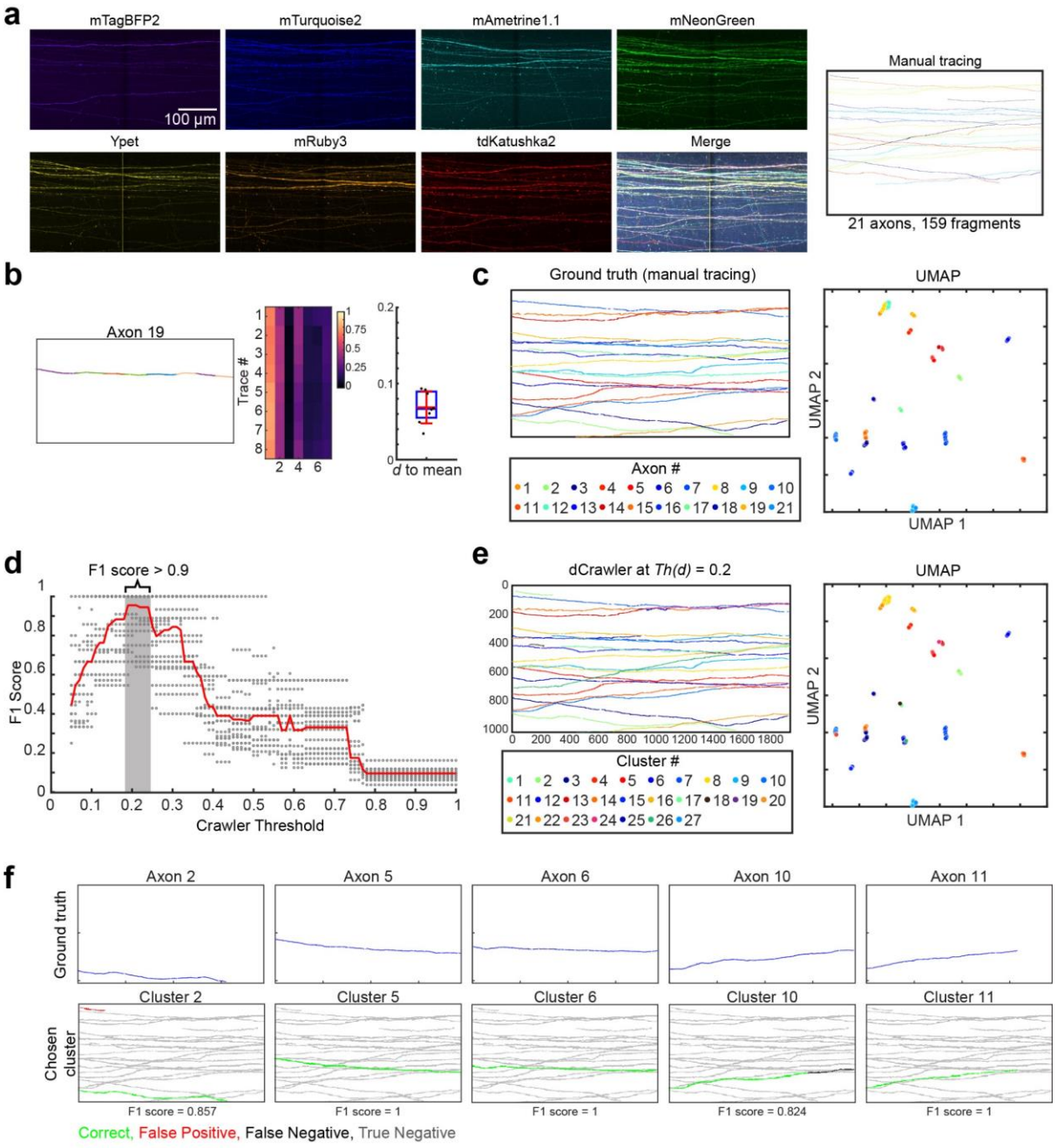

Extended Data Fig. 7 | Optimization for axonal reconstruction.

a, A 1 x 2 tiled image (A z-stacked image of 491.16 x 259.09 x 179.2 µm^3) of mitral and tufted cell axons were imaged at the lateral olfactory tract (left) and then manually traced using Neurolucida 360 (right). Image taken with a 20x objective lens.

b, A representative axon containing 8 fragments (left), their vector normalised colour vectors (middle), and the distance to the mean colour vector of the axon (right). See Supplementary Fig. 4 for all the results.

c, Ground truth of all the axons (manually traced). Left panel shows the location of fragments, while the right panel shows the location of these fragments in UMAP-reduced colour space.

d, The optimum threshold was calculated by running the dCrawler at a *d* ranging from 0.05 to 1. An F1 score was calculated for each axon at each *d* (gray dots), with the median F1 score for each *d* also displayed (red line). The optimum *d* was calculated to be 0.2.

e, The traces after clustering at the the optimum *Th(d)*, shown in physical space (a z-stacked image, left), and in UMAP-reduced colour space (right).

f, Representative neurons (blue lines, top row) paired to their best cluster (bottom row). Traces in both the neuron and the cluster are considered correct (green), those only in the cluster are a false positive (red), those in the neuron only as a false negative (black), and those in neither the neuron or cluster as a true negative (grey). See Supplementary Fig. 5 for all the results.

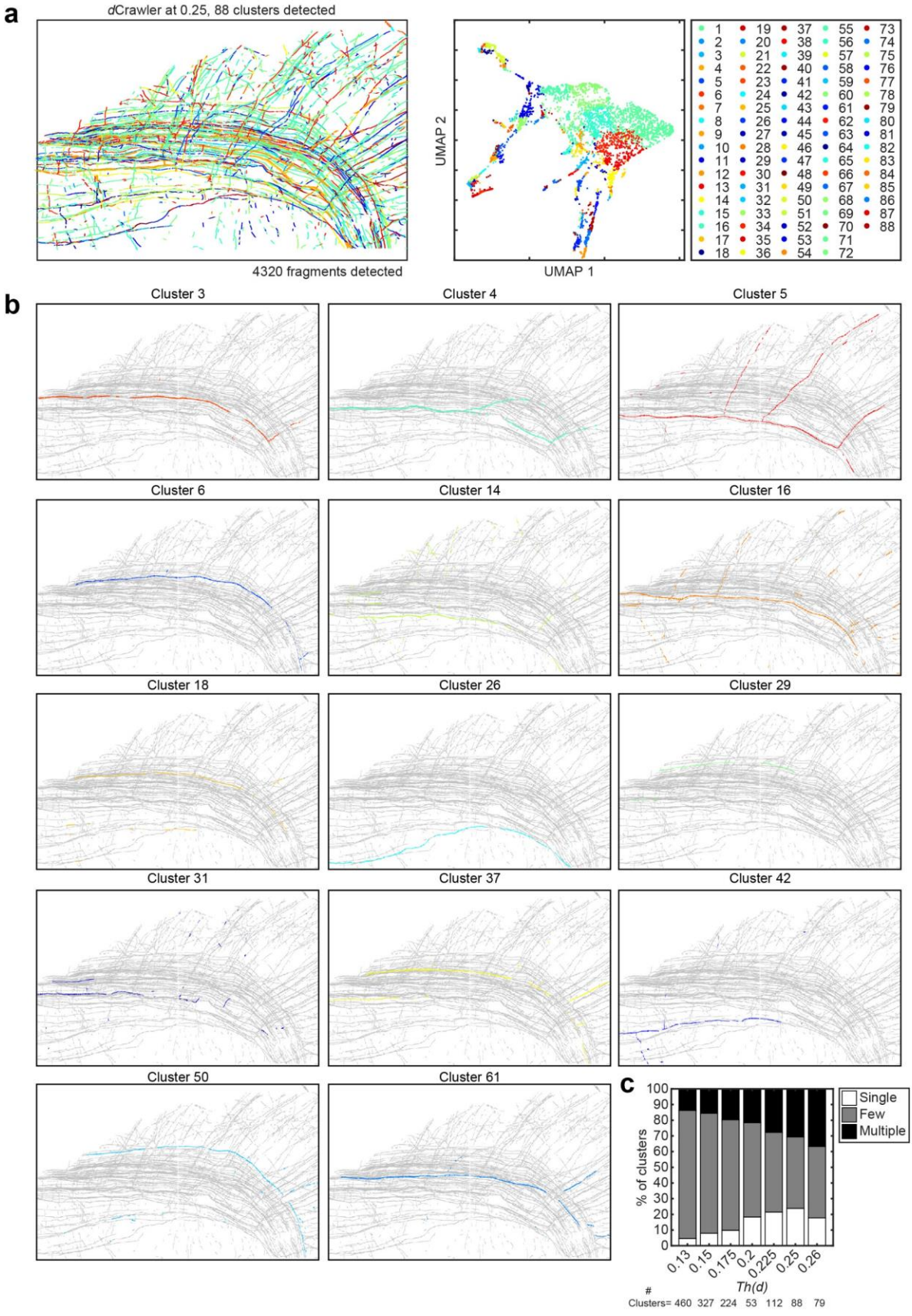

Extended Data Fig. 8 | Evaluation of mitral/tufted cell axons identified with QDyeFinder

a, All fragments detected automatically by Neurolucida360 in physical (left) and UMAP-reduced (right) space. Fragments are colour coded according to their cluster obtained when *Th(d)* = 0.25.

b, 14 clusters identified that seems to cover axons for a single neuron at *Th(d)* = 0.25.

c, Classification of dCrawler clusters at a range of *Th(d)* for mitral/tufted cell axon data. Clusters were grouped by whether a cluster contained a single neuron, multiple neurons, or few fragments. The best results were with *Th(d)* = 0.25.

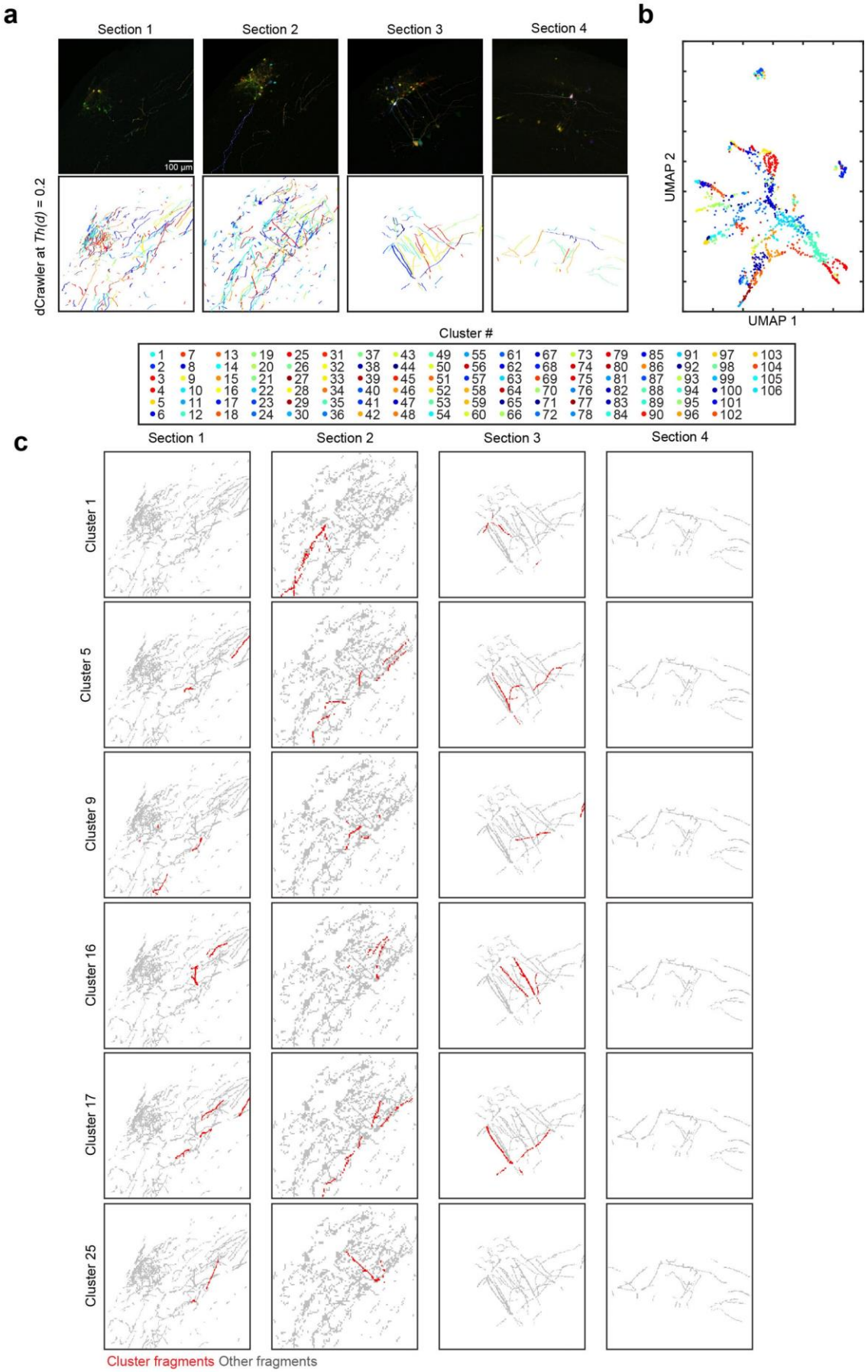

Extended Data Fig. 9 | Reconstruction of neurites across non-continuous samples

a, 7-color Tetbow AAV (with CAG-tTA) was injected into the olfactory bulb of wild-type C57BL/6N mice. Mitral/tufted cells and various types of periglomerular neurons are labelled. Four consecutive slices (100 μm thick) were cut with vibratome, cleared with SeeDB2G, and imaged with SeeDB2G. Top row shows z-stacked images (volume = 581.82 x 581.82 x 109 μm) for each of the four brain slices. The bottom row reflects the traces extracted by Neurolucida 360, colour-coded to reflect their corresponding cluster, after running QDyeFinder at $Th(d) = 0.2$.

b, All fragments represented in UMAP-reduced colour space, colours represent the cluster it is assigned by QDyeFinder.

c, Representative clusters which clearly belong to single neurons that span several brain sections. This suggests that provided acquisition parameters are constant colour vector alone is sufficient for reconstruction, without physical continuity.

Clustering Algorithm	**K-means clustering**	**Mean Shift Clustering**	**DBSCAN**	**dCrawler**
What it measures	Distance	Density	Density and distance	Distance
Input Required	Number of clusters	A density kernel	Minimum points and distance	A threshold distance
Advantage	Standard and fast	Outliers have very little effect	Considers both the density and distance of the points	Input doesn't require any assumptions on the spread of data
Disadvantage	We don't know the number of final clusters	The density of clusters may be variable	The clusters may be unevenly spread over space	Can produce too many clusters

Extended Data Table 1 | Comparison of unsupervised clustering algorithms

Supplementary Information

Supplementary Information contains following dataset.

Supplementary Fig. 1 | dCrawler description, related to Fig. 4.

Supplementary Fig. 2 | Evaluation of colour consistency in dendrites, related to Fig. 5b.

Supplementary Fig. 3 | Comparison of dCrawler clusters vs. ground truth for dendrites, related to Fig. 5f.

Supplementary Fig. 4 | Evaluation of colour consistency in axons, related to Extended Data Fig. 7.

Supplementary Fig. 5 | Comparison of dCrawler clusters vs. ground truth for axons, related to Extended Data Fig. 7.

Supplementary Video 1 | Visual representation of the dCrawler algorithm, related to Fig. 4.